

ICFO



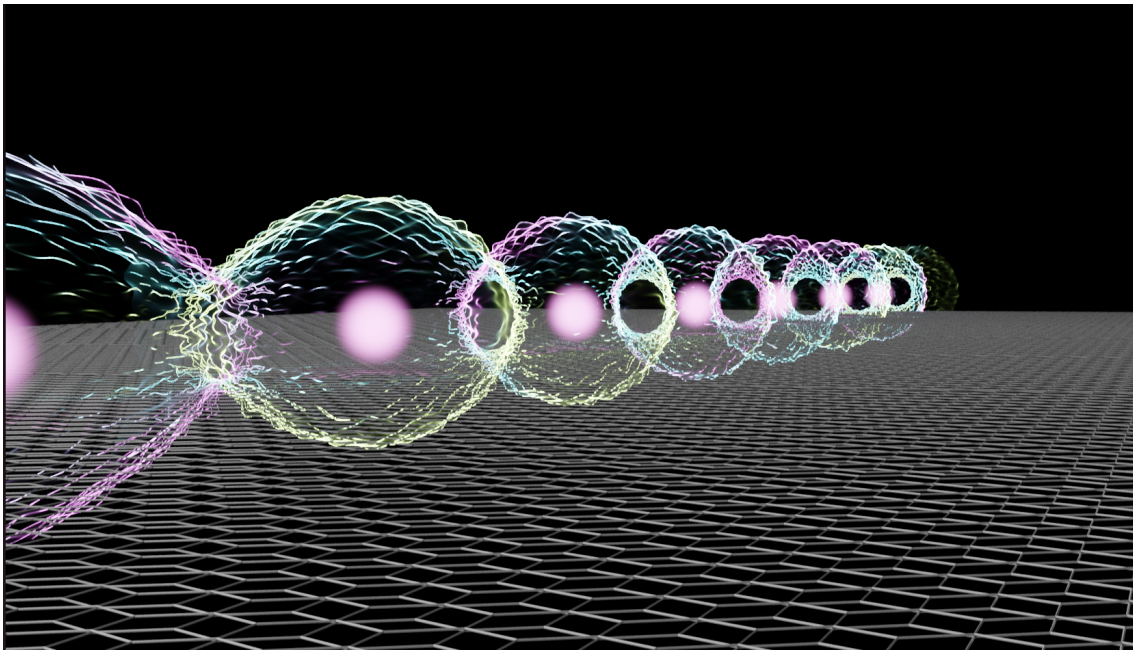
UAB
Universitat Autònoma
de Barcelona



MASTER IN QUANTUM SCIENCE AND TECHNOLOGY

MASTER'S THESIS

Numerical study of electrostatically-defined quantum dots in bilayer graphene



Author:
Sara Navarro

Supervisor:
Dr. Iacopo Torre

Institution:
ICFO-Institut de Ciències Fotòniques
Quantum nano-optoelectronics group.

10/07/2023

Numerical study of electrostatically-defined quantum dots in bilayer graphene

Sara Navarro

Supervised by: Iacopo Torre

ICFO-Institut de Ciències Fotòniques, The Barcelona Institute of Science and Technology, Av. Carl Friedrich Gauss 3, 08860 Castelldefels (Barcelona), Spain

10/07/2023

Interacting quantum many-body systems are so challenging to study that even simplified models, such as the Hubbard model, cannot be solved exactly. For this reason, it is interesting to engineer controllable quantum systems, called quantum simulators, that can emulate the behavior of these models. This makes quantum simulators a promising platform for studying the Hubbard model. These can be implemented, for example, using interacting arrays of quantum dots realized in semiconducting materials.

The capability to tune the bands in bilayer graphene with patterned gate electrodes provides an innovative platform to study such a model, as it is the first time to explore the Hubbard model with quantum dots in a two-dimensional material. Moreover, this platform opens a wide range of possibilities to study the different parameters of the model.

In this work, we study theoretically and numerically realistic models of electrostatically defined quantum dots in bilayer graphene. We can calculate the proposed device's potential and band-gap landscape induced in bilayer graphene by solving the Poisson equation. The result is then fed to a low-energy model to calculate the bound states of the quantum dots. This allows calculating the parameters of the corresponding Hubbard model, including tunneling amplitudes and on-site interactions. Our results can be directly used to design quantum-simulation devices based on quantum dots that are realized electrostatically in bilayer graphene.

Keywords: Quantum dots, Bilayer graphene, Quantum simulator, Hubbard model, Finite element method.

Contents

1	Introduction	3
1.1	Quantum simulators	3
1.2	Hubbard model	4
1.3	Gate-defined quantum dots in bilayer graphene using patterned gates	5
1.4	Objectives of the work	5
2	Electrostatic simulation of a bilayer graphene device	6
2.1	Poisson equation	7
2.2	Response of bilayer graphene	9
3	Single particle states of bilayer graphene under an inhomogeneous potential	11
3.1	Bilayer graphene under a central potential	12
3.1.1	Confined states in an artificial quantum dot	13
3.2	Extraction of Hubbard model parameters	14
3.2.1	Hubbard model parameters between states in a step-like central potential	15
3.3	Electronic band-structure of bilayer graphene under a periodic potential	17
3.3.1	Electronic band-structure of a square array of quantum dots in bilayer graphene	18
4	Conclusions	20
5	Supplementary material	20
	Bibliography	22
A	Properties of uniform bilayer graphene	26
B	Discretization of the eigenvalue/eigenvector equations for bilayer graphene under a radially symmetric potential using the finite element method	31
B.1	Obtaining the boundary conditions	31
B.2	Implementing the finite element method	32

1 Introduction

1.1 Quantum simulators

Quantum simulators (Qs) are controllable highly-interacting quantum many-particle systems. These devices use many-body interactions and entanglement to provide a new scientific approach to problems that cannot be solved with classical computation. The flexibility and wide definition of such systems involve applications in areas such as condensed-matter physics, quantum computing, chemistry, or cosmology [BN09, GAN14, ABC⁺21].

Quantum simulators are a promising tool for studying many-particle quantum systems [BN09]. In these systems, the number of parameters describing a quantum state grows exponentially with the size of the system N , which makes it infeasible to simulate them with a classical computer. Richard Feynman proposed, almost a half-century ago, using these real quantum mechanical devices to study quantum phenomena [Fey82].

Qs are usually classified into analog and digital quantum simulators [GAN14]. They differ in the way we try to reproduce a Hamiltonian H_{sys} that describes the dynamics of the quantum system under study. In analog quantum simulation, one directly maps the target Hamiltonian H_{sys} onto a quantum system we can easily access and control, and that is characterized by H_{sim} . This serves as a “toy model” of the real many-body system, from which we can extract valuable information, such as how the ground state and the dynamics of the system change when tuning H_{sim} . Alternatively, in digital quantum simulation, the unitary evolution of the state $U = e^{-iH_{sys}t}$ is replicated or approximated by applying unitary single-qubit or two-qubit operations to the initial state.

Thanks to recent scientific advances, it has been claimed that we are reaching the “golden era” of quantum simulation [ABC⁺21]. Yet we are far from reaching a general-purpose QS, as most of the platforms proposed serve to solve a specific problem. Therefore, when we talk about a concrete type of QS, whether this is used for analog or digital quantum simulation depends on the precise purpose of the experiment.

The most developed QS are ultracold atoms trapped in optical lattices [Cho23]. Their popularity lies in the capability to build and precisely measure large systems (also measuring different spins) and in their tunability, even *in situ* [BR12, TGU⁺12, GB17]. They have been proven to be useful to simulate interesting quantum many-body physics models, where a remarkable example is the Hubbard model.

Other types of Qs also explore this idea of trapping particles, which include ions, Rydberg atoms, or polar molecules, in periodic potentials. Other examples include superconducting circuits, atoms trapped in cavity arrays, optical tweezers, or different platforms using photons [GAN14].

Another tunable and versatile type of Qs are the arrays of interacting quantum dots (QDs) [BV13]. A QD is a nanometric semiconducting particle that has discrete quantum energy levels. Thus, they are commonly called artificial atoms. A QD can be obtained by confining charges in the three spatial directions in semiconducting materials, becoming effectively “zero-dimensional”. This is achieved by creating a spatially variable gap in the semiconductor. In this way, we construct quantum wells (or similar potentials where the energies are discretized), confining the charges. In Fig. 1, we have an explanatory scheme of a gap with a quantum well in a single spatial direction, showing the confined states in that direction. The effective zero-dimensional system would therefore be obtained when confining charges in all their free spatial directions. Experimentally, these kinds of gaps are obtained by implanting dopants in different regions of the semiconductor [SPP⁺16, WKF⁺22]; or by applying gate voltages to a two-dimensional (2D) electron gas, which are known as gate-defined quantum dots [vD21]. This work is focused on gate-defined quantum

dots since they provide a tunable platform for our QDs.

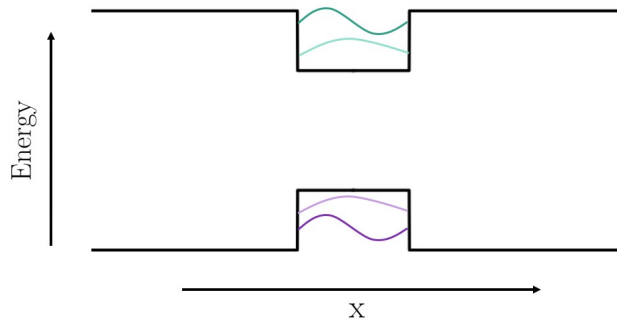


Figure 1: Scheme of a valence band and a conduction band of a semiconductor with a spatially variable gap in one spatial direction. We mark the confined states that could be created.

1.2 Hubbard model

One of the most important condensed matter models studied with QDs is the Hubbard model. The Hubbard model [Hub63] is a simplified model describing correlated electrons' behavior in a periodic potential. The Hamiltonian of those interacting electrons that can hop between a set of sites Λ is written as

$$\hat{H} = - \sum_{i,j \in \Lambda} \sum_{\sigma} t_{i,j} (\hat{c}_{i,\sigma}^{\dagger} \hat{c}_{j,\sigma} + \hat{c}_{j,\sigma}^{\dagger} \hat{c}_{i,\sigma}) + U \sum_{i \in \Lambda} \hat{n}_{i,\uparrow} \hat{n}_{i,\downarrow}, \quad (1)$$

where $\sigma = \uparrow, \downarrow$ represents the spin, $\hat{c}_{i,\sigma}^{\dagger}$ and $\hat{c}_{i,\sigma}$ are the creation and annihilation operators for a fermion with spin σ in site i and $\hat{n}_{i,\sigma} = \hat{c}_{i,\sigma}^{\dagger} \hat{c}_{i,\sigma}$ is the spin-density operator for a spin σ in site i . The two principal variables that define the Hamiltonian are $t_{i,j}$, which is the hopping parameter between sites i and j , and U , which is the on-site interaction. The ground state of the model is determined by the competition between these two parameters, which is essentially the relationship between the kinetic energy and interaction energy. Despite being a simplified model, it can not be in general solved numerically due to the exponential growth of the Hilbert space with the number of sites.

Consequently, the phase diagram of the model is still a field of study. Different phases appear when changing the parameters t and U . The extreme cases present a transition from the superfluid phase ($t \gg U$), where electrons are totally delocalized, to a Mott insulating phase ($U \gg t$), where electrons are fully localized in the lattice sites (see Fig. 2). The study of these quantum phases case has given a useful physical description to this still unknown phenomena in different fields, such as high-temperature superconductivity, magnetism, and charge density waves [Aue98].

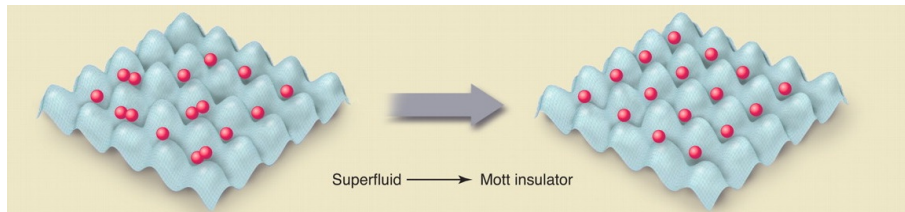


Figure 2: Scheme of the phase transition between the superfluid and the Mott insulator phase for ultracold neutral atoms in a 2D optical trap. Figure adapted from [BN09].

1.3 Gate-defined quantum dots in bilayer graphene using patterned gates

In the current work, we propose an analog quantum simulator to study the physics of the Hubbard model. The proposed platform consists of gate-defined quantum dots in bilayer graphene (BLG), where the shape of the electrostatic potential is defined by patterned gates. In this section, we explain in detail the main ideas under the presented experimental setup.

In gate-defined QDs, as mentioned above, the confinement of the charges is achieved by electrostatic gating, which offers more tunability compared to other QD platforms. Gate-defined QDs have been realized in BLG [MP08, EPP+18, BFE+18]. BLG is a 2D carbon-based material that consists of two stacked graphene layers. Unlike in monolayer graphene, one can open a band gap in BLG by applying a strong electric field in the normal direction to the BLG plane [McC06, OBS+06, OHL+07]. The size of the gap will depend on the strength of the electric field at each point. Consequently, one can combine layers of electrostatic split- and finger-gates to induce a spatially variant gap. Thus, we confine charge carriers in BLG creating electron and hole quantum dots. This technique enables the formation of single QDs as well as one-dimensional arrays of QDs [EPP+18, BFE+18, BMH+23].

An alternative approach of electrostatically confining charge carriers in BLG is patterning the gate electrode, thus inducing a locally varying potential. This approach has been used to create superlattices in single-layer graphene [PYS+08, HLC+20, BHH+22, KS23] and recently in BLG [GDA+23, SGW+23]. Extending this approach to BLG gives rise to single QDs dots as well as one- and two-dimensional arrays of QDs. These QD arrays create a platform for quantum simulation, whose underlying physical model is the Hubbard model [YWS11, KCX+21].

1.4 Objectives of the work

The aim of the current work is to completely characterize gate-defined QDs created using patterned gates in BLG. This will be done by providing a computational platform that obtains the response of BLG to a given superlattice potential and calculates the parameters that define the Hubbard Hamiltonian of that system. This will serve as theoretical support for the experiments, as it will help in the design of the devices and in the latter verification of the experimental results.

In this work, we approach the problem from two sides. First, in section 2, we obtain the electrostatic potential inside a device for a single quantum dot. Secondly, in section 3 we get the response of BLG to an arbitrary inhomogeneous radial potential that would create a single dot. Afterwards, we obtain the interaction parameters between two dots, from which the Hubbard parameters can be extracted. Then, the band structure of BLG under a superlattice potential is computed. Finally, we explain how to put together these two approaches to fully characterize our devices.

2 Electrostatic simulation of a bilayer graphene device

The goal of the project is to characterize QDs in BLG created by electrostatic gating using PGs that define the shape of the potential. The first step is to define and analyze the device that the experimental part of the project proposed, which is a device to create a single quantum dot that is scalable in order to create arrays of QDs. It is depicted in Fig. 3. Here, the BLG is encapsulated in insulating hexagonal Boron nitride (hBN). The contacts of this part of the device are a graphite back gate (BG) and top gate, being the top gate the PG. These materials are chosen to ensure the good quality of the device [DYM⁺10, WMH⁺13, EPP⁺18, IBW⁺22].

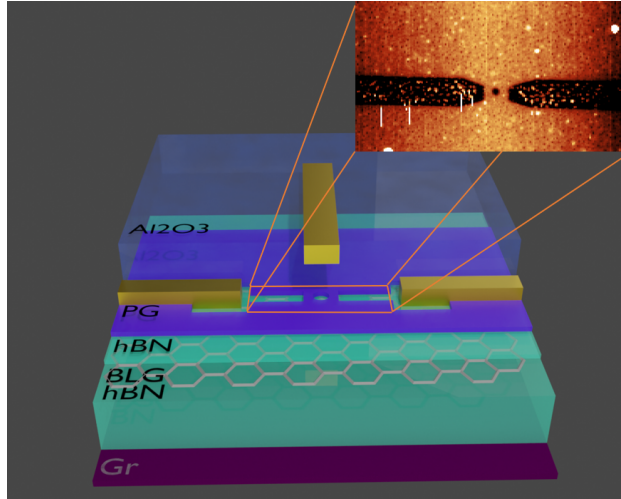


Figure 3: Scheme of a proposed device showing the different layers and materials composing it. In the inset, atomic force microscope scan of a real device. Courtesy of Rebecca Hoffmann.

In the inset of Fig. 3 the shape of a real PG is represented. We see that it has a circular-shaped hole in the middle, which would create a central potential where the electrons would be confined. The two “arms” serve to occupy the QD. Lastly, separated by an alumina (Al_2O_3) layer¹, we put a gold finger-like gate (GG) to change the potential energy inside the dot, controlling the occupation.

In this device, there are several variables that can influence the shape of the electrostatic potential around the dot and, subsequently, the characteristics of the resultant QD. Therefore, we seek a platform to characterize these QDs that permits easy tuning of those different variables, which include the potential applied in the gates, the width of the layers, or the parameters that fix the shape of the PG. This flexible platform would facilitate the design of the sought device.

In this section, we describe the first step to characterize the QDs, which is to obtain the shape of the electrostatic potential inside the device. In order to do that, we obtain the first approach to the electrostatic potential by solving the Poisson equation without free charges. Then, we describe how to take into account the response of BLG to this potential to get a better approximation.

¹In this case alumina is chosen for simplicity.

2.1 Poisson equation

We aim to obtain the electrostatic potential's value inside the device when we apply certain voltages on the gates. Thus, we must solve the Poisson equation for the electrostatic potential ϕ

$$-\nabla \cdot (\boldsymbol{\epsilon} \cdot \nabla \phi) = 4\pi \varrho_{free}, \quad (2)$$

where $\boldsymbol{\epsilon}$ is the matrix of permittivity of the considered material and ϱ_{free} are the free charges. The boundary conditions will be determined by the voltages applied to the different metallic gates (the BG, PG, and GG). They read

$$\begin{aligned} \phi(x, y, z_{BG}) &= V_{BG} \\ \phi(x, y, z_{PG}) &= \begin{cases} V_{PG} & \text{If } (x, y) \in \text{Patterned gate} \\ \text{Not fixed} & \text{Otherwise} \end{cases} \\ \phi(x, y, z_{GG}) &= \begin{cases} V_{GG} & \text{If } (x, y) \in \text{Golden gate} \\ \text{Not fixed} & \text{Otherwise} \end{cases} \end{aligned} \quad (3)$$

where the different z correspond to the positions of the different gates. In the edges of the geometry, we choose homogeneous Von Neumann boundary conditions

$$\frac{\partial \phi(\mathbf{x})}{\partial \mathbf{n}} = 0 \quad \text{if } \mathbf{x} \in \text{edges}, \quad (4)$$

where \mathbf{n} denotes the vector in the normal direction to the surface. This condition will be appropriate providing that we choose a sufficiently large simulation volume.

We solve the stated problem for the electrostatic potential using the Finite Element Method (FEM), which is a numerical method for partial derivatives equations. To implement the method, we divide our space into finite elements, a concrete discretization where we create a mesh of our object. The FEM then solves what is called the *weak form* of a given boundary-value problem. The weak form of Eq. 2 in a spatial domain Ω (which, considering our problem, we choose to be a volume) reads

$$-\int_{\Omega} dV \nabla \cdot (\boldsymbol{\epsilon} \cdot \nabla \phi) v = \int_{\Omega} dV 4\pi \varrho_{free} v, \quad (5)$$

where v is called *test function* and dV is the differential element of our domain. We require Eq. 5 to hold $\forall v \in \hat{V}$, being \hat{V} the *test space*. Therefore, the resulting mathematical problem determines uniquely $\phi \in V$, where V is called the *trial space*. To facilitate the computation of the problem and as it is normally done in variational formulation, it is convenient to reduce the order of the derivatives. Thus, we rewrite Eq. 5 using the integration by parts and using the divergence theorem, which leads to

$$-\iint_{S(\Omega)} dS (\hat{\mathbf{n}} \cdot \boldsymbol{\epsilon} \cdot \nabla \phi) v + \int_{\Omega} dV \nabla v \cdot \boldsymbol{\epsilon} \cdot \nabla \phi = \int_{\Omega} dV 4\pi \varrho_{free} v. \quad (6)$$

If we consider the boundary conditions explained before, the first term on the left side of Eq. 6 vanishes [LM]. Moreover, in this first approximation, we will consider there are no free charges ($\varrho_{free} = 0$)². The equation we need to solve then reduces to

$$\int_{\Omega} dV \nabla v \cdot \boldsymbol{\epsilon} \cdot \nabla \phi = 0. \quad (7)$$

²In section 2.2, we will see why this is only the first approximation; and how the problem must be solved recursively.

Therefore, to characterize the electrostatic potential inside the device, we solve Eq. 7 being our domain Ω the volume inside the device. Hence, we must generate the mesh of the device. This is done using the 3D finite element mesh generator `gmsh` [GR09], which is available in Python via a package with the same name. This enables keeping all the parameters that define the geometry of the device as variables for the user to choose (see Figs. 4a and 4b). The mesh also contains specific tags so that we can distinguish between the different parts of the device, which is crucial to specify the dielectric constant of each material or to identify the gates. The size of the finite elements can also be chosen, which enables us to choose the time/precision ratio, as the higher the precision the longer the calculations take. In other words, we create a flexible platform to try different values for the variables for the created geometry.

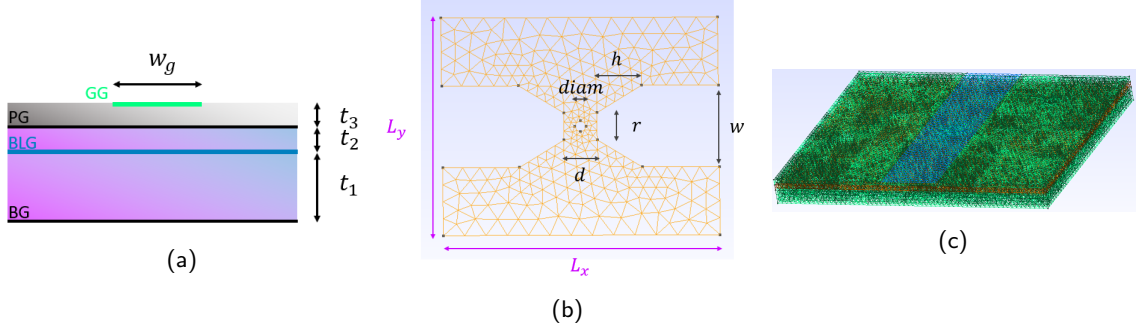


Figure 4: Schemes of the **(a)** lateral view and **(b)** top view of the patterned gate for the proposed device. All the indicated distances correspond to the parameters we are able to tune in order to create the mesh of the device. **(c)** Example of a mesh for the geometry of the proposed device.

Once having the mesh, we use the Python package `diffusive_solver` [Tor20, Tora] to obtain the electrostatic potential ϕ and the displacement field D_i (where $i = x, y, z$ is the direction of the field). `Diffusive_solver` is a package for solving diffusion problems that is based in FEniCS [Log12, ABH⁺15], another Python package for solving partial differential equations using the FEM. From the resultant ϕ and D_z , we obtain the physical quantities that are of our interest when calculating the response of BLG to the potential. These are the potential energy V and the interlayer asymmetry Δ , which is the difference of energy between the BLG layers. They can be obtained using the relations

$$\begin{aligned} V &= -e\phi \\ \Delta &= et_z D_z \end{aligned} \quad (8)$$

where e is the fundamental charge, $t_z = 3.4\text{\AA}$ [Wal47] is the distance between BLG layers and D_z is the displacement field in the z direction.

We now provide an example of a calculation. The parameters describing the device used were proposed by the experimental group working on these devices and can be found in the supplementary material (see section 5). The mesh used to perform these calculations is the one in Fig. 4c. We solve the boundary condition problem by fixing the voltages arbitrarily (with values of $V_{BG} = 0\text{V}$, $V_{PG} = 2\text{V}$, and $V_{GG} = -3\text{V}$). Finally, we plot different views of the potential energy and the interlayer asymmetry in Figs. 5.

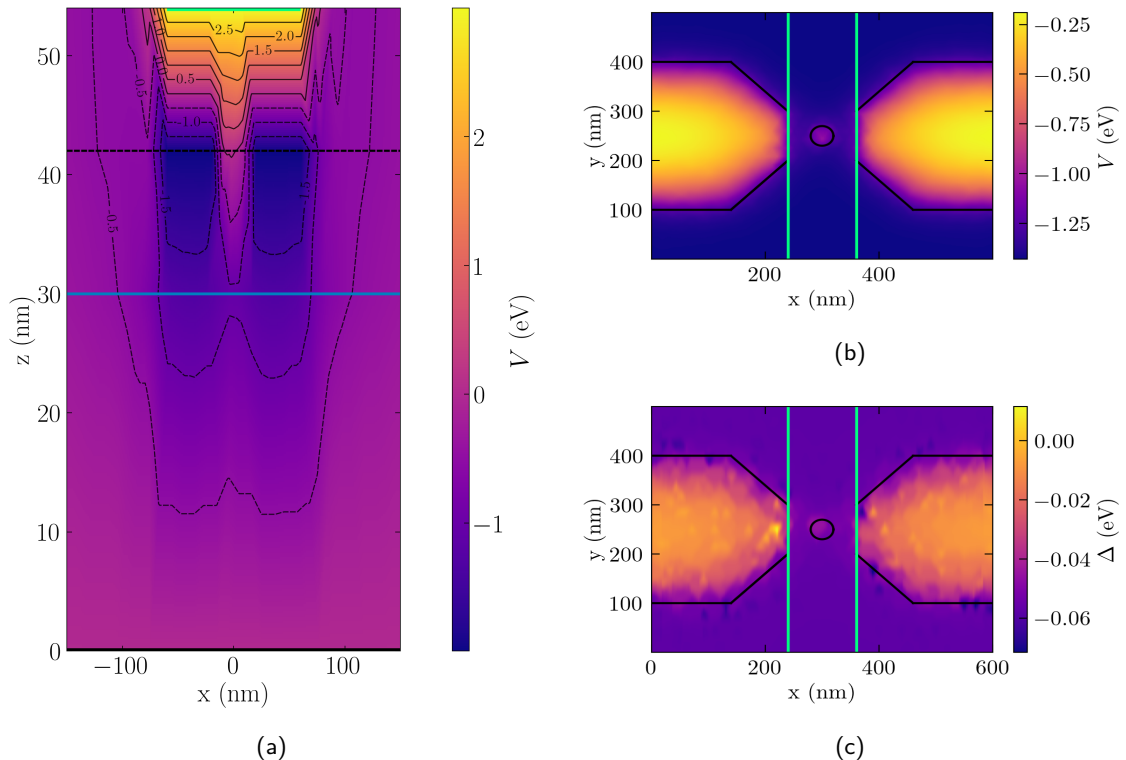


Figure 5: Plots of the different electrostatic parameters in our device for the considered examples. In the first two figures, we plot the potential energy V in **(a)** the xz plane, for a value of y that passes through the center of the hole and in **(b)** the xy plane in the position of BLG ($z = z_{BLG}$). In **(c)**, we plot the interlayer asymmetry in the same way we have done in **(b)**. In **(a)**, the solid and dashed black lines represent the graphite BG and PG, respectively; the blue line is the BLG; and the green line is the GG. Alternatively, in **(b)** and **(c)** the black lines represent the shape of the PG while the green lines are again the GG.

2.2 Response of bilayer graphene

In the previous section, we obtained the shape of the electrostatic potential in the absence of free charges. Nevertheless, applying a field to BLG changes its charge configuration, which results in non-null charge density on the top (ρ_+) and bottom layer (ρ_-). Thus, the total charge density $\rho = \rho_+ + \rho_-$ and the polarization density $P_z = t_z(\rho_+ - \rho_-)/2$ of BLG change when a potential is applied. Their values will depend on the chemical potential μ and in the interlayer asymmetry Δ , which are parameters that are extractable from the calculations done (note that $-e\phi + \mu = -eV$, where V is the electrochemical potential). The calculation of these parameters on BLG under a homogeneous potential is done in the appendix [A](#).

Since applying an electrostatic potential to BLG displaces the charges in the layers, we can no longer assume that there are no free charges. Thus the initially solved problem changes, and, in order to get the exact electrostatic potential in the device, the equations must be solved recursively taking into account the response of BLG in each iteration. Assuming that the only free charges are the ones appearing in BLG, we can still consider Eq. [7](#) in the whole device except for the BLG, and consider the effect of BLG by imposing some boundary conditions in the top and bottom layers. These boundary conditions must

fulfill the equations

$$D_{z+} - D_{z-} = 4\pi\rho, \quad (9)$$

$$\frac{D_{z+} + D_{z-}}{2} = \frac{4\pi P_z}{t_z} + \frac{\Delta}{et_z}, \quad (10)$$

where D_{z+} and D_{z-} are the displacement fields in the positive z direction in the top and bottom layers, respectively, and we use the definition of the interlayer asymmetry as a function of $\phi(z)$ that we present in the next section, in Eq. 13.

As an approximation, we will consider that the relation between the charge density and the polarization and the potential. is that of BLG in a homogeneous potential. These relationships are the ones obtained in appendix A, in concrete, expressed in Eqs. 67 and 68.

We now proceed to analyze the response of BLG under an inhomogeneous potential. This potential would be the one obtained after recursively solving the equation for the electrostatic problem. Nonetheless, we will just stick to an arbitrary central potential as we have not obtained the real electrostatic potential yet. This will serve us to characterize the dots and obtain the interactions between them.

3 Single particle states of bilayer graphene under an inhomogeneous potential

In this work, we consider Bilayer graphene in its most energetically stable type of stacking, which is the AB-stacking, also known as Bernal stacking [YPZ⁺11]. BLG is a semimetal, and the conduction and valence bands meet in the high symmetry points K_+ and K_- , which are the corners of the first Brillouin zone.

Close to the point K_ξ (where ξ is the valley index and can take the values of $\xi = \pm 1$), the highest valence band and the lowest conduction band can be described with a low-energy effective Hamiltonian [MK13]

$$\mathcal{H}_{0\xi}(\mathbf{k}) = -\frac{\hbar^2}{2m} \begin{pmatrix} 0 & (\boldsymbol{\pi}^\dagger)^2 \\ \boldsymbol{\pi}^2 & 0 \end{pmatrix}, \quad (11)$$

where $\boldsymbol{\pi} = \xi k_x + ik_y$, $\boldsymbol{\pi}^\dagger = \xi k_x - ik_y$, \mathbf{k} is the crystal momentum measured from K_ξ , and m is the effective mass of the carriers in BLG and has a value of $0.03m_e$ [ZHZ11], where m_e is the electron mass.

Since in all the situations studied in our work the valley symmetry is preserved, we will consider only the $\xi = 1$ valley and then take into account the presence of the other valley via a degeneracy factor $g_v = 2$. In the same way, the spin symmetry is also conserved, giving a degeneracy $g_s = 2$. Our electronic system has therefore a total degeneracy of $g = g_s g_v = 4$.

Applying an electrostatic potential $\phi(z)$ which is uniform in the in-plane directions produces a new term in the Hamiltonian

$$\mathcal{H}_{\text{pot}} = \begin{pmatrix} V + \frac{\Delta}{2} & 0 \\ 0 & V - \frac{\Delta}{2} \end{pmatrix}, \quad (12)$$

where V is the average potential energy and Δ is the interlayer asymmetry. Calling z_+ and z_- to the coordinates of the top and bottom layers, respectively, V and Δ can be calculated from $\phi(z)$ as:

$$\begin{aligned} V &= -e \frac{[\phi(z_+) + \phi(z_-)]}{2}, \\ \Delta &= -e[\phi(z_+) - \phi(z_-)]. \end{aligned} \quad (13)$$

The response of BLG under such a uniform potential is described in appendix A.

We can obtain the low-energy effective model that describes the eigenstates of BLG under an **inhomogeneous electrostatic potential** by promoting \mathbf{k} to an operator via the substitution $\mathbf{k} \rightarrow \hat{\mathbf{p}}/\hbar = -i\nabla$ and allowing V and Δ to depend on the position operator $\hat{\mathbf{r}}$. This gives the effective Hamiltonian that we will use in the remainder of this chapter

$$\mathcal{H} = -\alpha \begin{pmatrix} 0 & (\hat{\boldsymbol{\pi}}^\dagger)^2 \\ \hat{\boldsymbol{\pi}}^2 & 0 \end{pmatrix} + \begin{pmatrix} \frac{\Delta(\hat{\mathbf{r}})}{2} + V(\hat{\mathbf{r}}) & 0 \\ 0 & -\frac{\Delta(\hat{\mathbf{r}})}{2} + V(\hat{\mathbf{r}}) \end{pmatrix}, \quad (14)$$

where $\alpha = \hbar^2/(2m) \approx 1.27 \text{ eV} \cdot \text{nm}^2$ and $\hat{\boldsymbol{\pi}} = (\hat{p}_x + i\hat{p}_y)/\hbar$.

In the next section, we will solve the time-independent Schrödinger equation for the Hamiltonian in Eq. 14 with an arbitrary central potential and focus on its bound eigenstates. Then, we will calculate the Hubbard model parameters (superposition, tunneling, and Coulomb interaction) for those states as a function of the distance between the sites. Finally, obtain the band structure for the Hamiltonian 14 when the applied potential is periodic.

3.1 Bilayer graphene under a central potential

In this section, we solve the time-independent Schrödinger equation $\mathcal{H}\Psi(\mathbf{r}) = E\Psi(\mathbf{r})$, where \mathcal{H} is given by Eq. 14, with central potentials $V(\rho)$ and $\Delta(\rho)$. Thus, it is convenient to use polar coordinates, such that the operators $\hat{\pi}$ and $\hat{\pi}^\dagger$ become

$$\hat{\pi}^2 = e^{+2i\theta} \left(-\frac{\partial^2}{\partial \rho^2} + \frac{1}{\rho^2} \frac{\partial^2}{\partial \theta^2} + \frac{1}{\rho} \frac{\partial}{\partial \rho} + \frac{2i}{\rho^2} \frac{\partial}{\partial \theta} - \frac{2i}{\rho} \frac{\partial^2}{\partial \rho \partial \theta} \right), \quad (15)$$

$$\left(\hat{\pi}^\dagger\right)^2 = e^{-2i\theta} \left(-\frac{\partial^2}{\partial \rho^2} + \frac{1}{\rho^2} \frac{\partial^2}{\partial \theta^2} + \frac{1}{\rho} \frac{\partial}{\partial \rho} - \frac{2i}{\rho^2} \frac{\partial}{\partial \theta} + \frac{2i}{\rho} \frac{\partial^2}{\partial \rho \partial \theta} \right). \quad (16)$$

Due to the rotational symmetry, since we can separate the radial and the angular part of the wavefunction, we introduce the ansatz

$$\Psi(\mathbf{r}) = \sum_{\ell=-\infty}^{\infty} e^{i\ell\theta} \begin{pmatrix} f_\ell^+(\rho) \\ f_\ell^-(\rho) \end{pmatrix}, \quad (17)$$

where $\ell \in \mathbb{Z}$ is the angular quantum number. We see in Eqs. 15 and 16 that the operators $\hat{\pi}^2$ and $\left(\hat{\pi}^\dagger\right)^2$ couple angular quantum numbers that differ by 2. Consequently, we find it convenient to rewrite Eq. 17 in the form:

$$\Psi(\mathbf{r}) = \sum_{\ell=-\infty}^{\infty} e^{i\ell\theta} \begin{pmatrix} f_{\ell-1}^+(\rho) e^{-i\theta} \\ f_{\ell+1}^-(\rho) e^{i\theta} \end{pmatrix} = \sum_{\ell=-\infty}^{\infty} e^{i\ell\theta} \begin{pmatrix} u_{\ell,+}(\rho) e^{-i\theta} \\ u_{\ell,-}(\rho) e^{i\theta} \end{pmatrix}, \quad (18)$$

where we have defined $u_{\ell,\pm}(\rho) \equiv f_{\ell\mp 1}^\pm(\rho)$. With these substitutions, the Schrödinger equation for the radial part of $\Psi(\mathbf{r})$ reduces to the system of equations

$$\alpha \left[\ddot{u}_{\ell,-}(\rho) + \frac{1+2\ell}{\rho} \dot{u}_{\ell,-}(\rho) + \frac{\ell^2-1}{\rho^2} u_{\ell,-}(\rho) \right] + \left[V(\rho) + \frac{\Delta(\rho)}{2} \right] u_{\ell,+}(\rho) = E u_{\ell,+}(\rho), \quad (19)$$

$$\alpha \left[\ddot{u}_{\ell,+}(\rho) + \frac{1-2\ell}{\rho} \dot{u}_{\ell,+}(\rho) + \frac{\ell^2-1}{\rho^2} u_{\ell,+}(\rho) \right] + \left[V(\rho) - \frac{\Delta(\rho)}{2} \right] u_{\ell,-}(\rho) = E u_{\ell,-}(\rho), \quad (20)$$

where the dot stands for the derivative with respect to ρ .

For the solutions to behave well at $\rho = 0$, the following boundary conditions (BC) must be imposed (see details in appendix B.1):

$$\text{if } \ell \neq \pm 1 : u_{\ell,\pm}(\rho = 0) = 0; \quad (21)$$

$$\text{if } \ell = +1 : \dot{u}_{+1,+}(\rho = 0) = 0, \quad u_{+1,-}(\rho = 0) = 0; \quad (22)$$

$$\text{if } \ell = -1 : \dot{u}_{-1,-}(\rho = 0) = 0, \quad u_{-1,+}(\rho = 0) = 0. \quad (23)$$

On the other hand, since the $u_{\ell,\pm}$ must be square integrable in all the space, they must decay as $\rho \rightarrow \infty$.

In general, these equations cannot be solved analytically and numerical approaches must be done. These numerical solutions are obtained by discretizing the equations using the finite element method. We describe the discretization in appendix B and implement it in the Python package `cylindrical_waveequations` [NT], which obtains the corresponding eigenstates and eigenenergies for any given $V(\rho)$ and $\Delta(\rho)$.

The precision of the numerical solutions depends on two variables that appear when discretizing our equations: ρ_{max} and N . ρ_{max} is the maximum value considered for the radial variable. It must be big enough in order to correctly capture the decay of the

functions as $\rho \rightarrow \infty$ (which is done by imposing the BC $u_{\ell,\pm}(\rho_{max}) = 0$). On the other hand, N is the number of parts in which we divide our domain $\rho \in [0, \rho_{max}]$. It will define the precision of our solution, where the error decays as a power law with N . Also note that the bigger ρ_{max} is, the greater N we need to reach the same precision. However, setting high numbers for these variables also increases the computational time and memory needed.

3.1.1 Confined states in an artificial quantum dot

In this section, we obtain the confined eigenstates and eigenenergies of a potential. A potential that allows confined states with discrete energy levels will be an artificial quantum dot. The general form reads

$$V(\rho) = V_{\text{dot}}(\rho) + V_{\text{out}}, \quad (24)$$

$$\Delta(\rho) = \Delta_{\text{dot}}(\rho) + \Delta_{\text{out}}. \quad (25)$$

In the current example, we consider a radial interlayer asymmetry square well of radius ρ_0 and depth Δ_{well} by taking $\Delta_{\text{dot}}(\rho) = -\Delta_{\text{well}}\theta(\rho_0 - \rho)$. We choose $\Delta_{\text{well}} = 25\text{meV}$, $\Delta_{\text{out}} = 50\text{meV}$ and $\rho_0 = 20\text{nm}$. Regarding the average potential, for simplicity, we will set $V_{\text{dot}} = 0$ because it is not as important as the interlayer asymmetry when creating the artificial dots and we will consider symmetric bands by fixing $V_{\text{out}} = 0$. Lastly, the chosen parameters for the discretization are $\rho_{max}=500$ and $N=5000$.

We solve the eigenenergy/eigenfunction problem for the described potential and identify the confined states, which we know correspond to the eigenenergies that lie inside the well. We observe that the only angular quantum numbers ℓ that allow these states are $\ell = 0, \pm 1, \pm 2$, where there are 2 confined states for $\ell = 0$ and a single one for each of the remaining ℓ s. We will refer to the energies lower/upper bands with $n = -1/1$. Thus, each state will be determined by the quantum numbers $[\ell, n]$. We plot the mentioned bound energies in Fig. 6 and summarize their energetic values in table 1. Besides, the confined wavefunctions corresponding to those states are plotted in Figs 7.

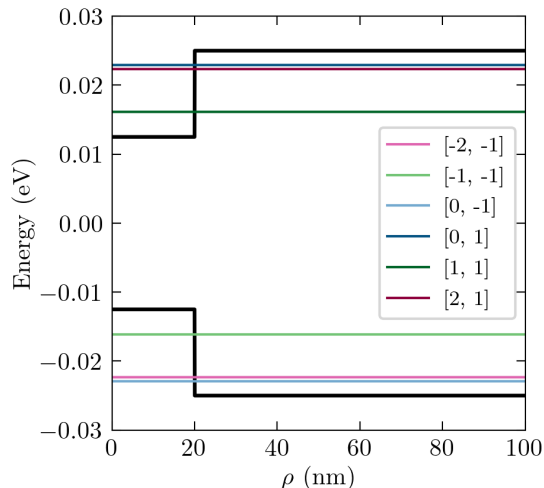


Figure 6: Energies of the confined states with quantum numbers $[\ell, n]$ for the step-like central Δ_{dot} . In black, we plot $V(\rho) \pm \frac{\Delta(\rho)}{2}$ as a function of ρ .

n	$\ell = -2$	$\ell = -1$	$\ell = 0$	$\ell = 1$	$\ell = 2$
-1	-22.324	-16.125	-22.911	—	—
1	—	—	22.911	16.125	22.324

Table 1: Values of the energies (in meV) for the confined states for the different quantum numbers ℓ and n .

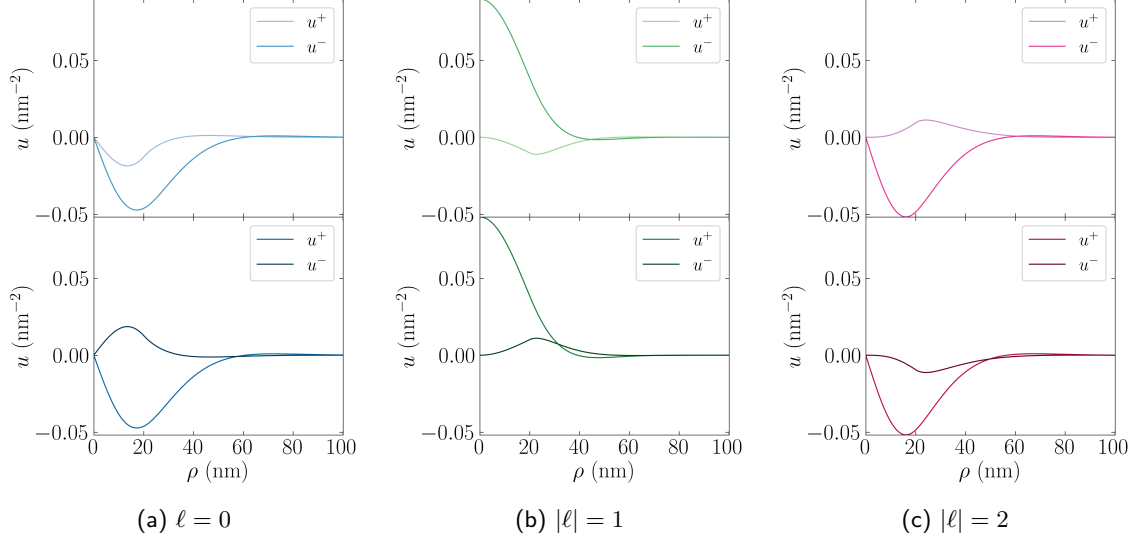


Figure 7: Confined states for the different $|\ell|$ as a function of the radial coordinate ρ for the step-like central Δ_{dot} . The wavefunctions above correspond to the states in the valence band ($n = -1$) and below correspond to the ones in the conduction band ($n = 1$). For each $[\ell, n]$, we plot $u^{\pm} \equiv u_{\ell, \pm}$.

3.2 Extraction of Hubbard model parameters

We are interested in using arrays of electrostatically defined quantum dots in BLG as a quantum simulator of the Hubbard model. In order to obtain the Hubbard Hamiltonian that describes our system, we need to consider two dots at a relative position fixed by a vector \mathbf{R} . Each dot will be defined by its corresponding eigenfunction $\psi_{\ell, n}$. The different interactions between the confined states will fully define the parameters of the Hubbard model, where the overlap, the crystal field integral, and the tunneling define the tight-binding part of the model, while the Coulomb interaction defines the on-site interaction.

The tight-binding parameters serve to build the effective tight-binding Hamiltonian of the system. They are called and defined as [Ash76] **overlap integral**

$$\alpha_{\ell_1, n_1, \ell_2, n_2}(\mathbf{R}) = \int d^2\mathbf{r} \psi_{\ell_1, n_1}(\mathbf{r})^\dagger \psi_{\ell_2, n_2}(\mathbf{r} - \mathbf{R}), \quad (26)$$

crystal field integral

$$\beta_{\ell_1, n_1, \ell_2, n_2}(\mathbf{R}) = - \int d^2\mathbf{r} \psi_{\ell_1, n_1}(\mathbf{r}) \nabla_{\text{dot}}(\mathbf{r} - \mathbf{R}) \psi_{\ell_2, n_2}(\mathbf{r}), \quad (27)$$

and **tunneling integral**

$$\gamma_{\ell_1, n_1, \ell_2, n_2}(\mathbf{R}) = - \int d^2\mathbf{r} \psi_{\ell_1, n_1}(\mathbf{r}) \nabla_{\text{dot}}(\mathbf{r} - \mathbf{R}) \psi_{\ell_2, n_2}(\mathbf{r} - \mathbf{R}), \quad (28)$$

where

$$\mathbb{V}_{\text{dot}}(\mathbf{r}) = \begin{pmatrix} V_{\text{dot}}(\rho) + \frac{\Delta_{\text{dot}}(\rho)}{2} & 0 \\ 0 & V_{\text{dot}}(\rho) - \frac{\Delta_{\text{dot}}(\rho)}{2} \end{pmatrix}. \quad (29)$$

The dependence on the angular part of \mathbf{R} (θ_R) of the tight binding parameters can be simplified by noting the relation

$$\alpha_{\ell_1, n_1, \ell_2, n_2}(R, \theta_R) = e^{i(\ell_2 - \ell_1)(\theta_R - \theta_{R_0})} \alpha_{\ell_1, n_1, \ell_2, n_2}(R, \theta_{R_0}), \quad (30)$$

which also holds for the crystal field integral β and the tunneling γ .

Moving to the Coulomb interaction, we will consider both the interaction between electrons in the same dot (on-site) and the interaction between neighboring dots (off-site). The **on-site Coulomb interaction energy** can be described as

$$U_{\ell_1, n_1, \ell_2, n_2} = \frac{1}{2} \int d^2\mathbf{r} n_{\ell_1, n_1}(\mathbf{r}) V_{\ell_2, n_2}(\mathbf{r}), \quad (31)$$

where $n(\mathbf{r})$ is the electron density at \mathbf{r} and $V(\mathbf{R})$ is the Coulomb potential created by the total electron density $n(\mathbf{r})$ at point \mathbf{R} . As the potential is radial, these will not have angular dependence. The electron density reads

$$n_{\ell, n}(\mathbf{r}) = \psi^\dagger(\mathbf{r})_{\ell, n} \psi(\mathbf{r})_{\ell, n} = \frac{1}{2\pi} \left(|u_{\ell, n}^+(\rho)|^2 + |u_{\ell, n}^-(\rho)|^2 \right) = n_{\ell, n}(\rho) \quad (32)$$

and the Coulomb potential created by $n_{\ell, n}(\mathbf{r})$ (noting that, due to the symmetry we can omit the angular part of \mathbf{R} , θ_R)

$$\begin{aligned} V_{\ell, n}(\mathbf{R}) &= e^2 \int d\mathbf{r} \frac{n_{\ell, n}(\mathbf{r})}{|\mathbf{r} - \mathbf{R}|} = e^2 \int_0^\infty \rho d\rho n_{\ell, n}(\rho) \int_{-\pi}^\pi d\theta \frac{1}{\sqrt{\rho^2 + R^2 - 2\rho R \cos(\theta)}} \\ &= e^2 \int_0^\infty \rho d\rho n_{\ell, n}(\rho) \frac{4}{\rho + R} K\left(\frac{4\rho R}{(\rho + R)^2}\right) = V_{\ell, n}(R), \end{aligned} \quad (33)$$

where $K(m)$ is the elliptic integral of the first kind, defined as

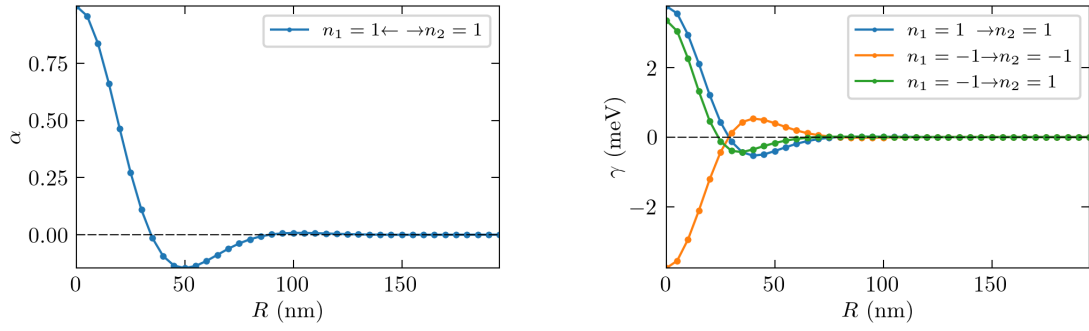
$$K(m) = \int_0^{\frac{\pi}{2}} [1 - m \sin^2 \theta]^{-\frac{1}{2}} d\theta. \quad (34)$$

Lastly, the **offsite Coulomb interaction energy** is

$$U_{\ell_1, n_1, \ell_2, n_2}(\mathbf{R}) = \frac{1}{2} \int d^2\mathbf{r} n_{\ell_1, n_1}(\mathbf{r}) V_{\ell_2, n_2}(\mathbf{r} - \mathbf{R}). \quad (35)$$

3.2.1 Hubbard model parameters between states in a step-like central potential

In this section, we obtain the Hubbard model parameters between two QDs with relative position \mathbf{R} , being these QDs the ones studied in section 3.1.1. We start by calculating the overlap and tunneling between states with $\ell = 0$. The crystal integral is ignored because its effect is negligible. We see in Figs. 8 the non-null and non-repeated interactions as a function of the distance between sites and for any θ_R (since the results have no angular dependence as we note from Eq. 30). Moreover, in tables 2 and 3 we summarize all the possible overlaps and tunnelings between the QDs, distance with the maximum interaction values ($R = 50\text{nm}$), and choose $\theta_R = 0$.



(a) Overlap between $n_1 = 1$ and $n_2 = 1$. The case $n_1 = -1 \leftrightarrow n_2 = -1$ is equivalent. The rest of the cases vanish.

(b) Tunneling between the different combinations of n_1 and n_2 . Case $n_1 = -1 \rightarrow n_2 = 1$ is equivalent to $n_1 = 1 \rightarrow n_2 = -1$.

Figure 8: Interaction parameters for $\ell = 0$ as a function of the distance between sites R .

$\ell_1 \backslash \ell_2$		n_2		0		1	2
		-2	-1	-1	1	1	1
-2	-1	-0.140	-0.096	-0.240	0.003	-0.007	0.000
	1	0.096	-0.002	0.124	-0.002	0.000	-0.007
-1	-1	-0.240	-0.124	-0.146	0.000	-0.002	-0.003
	1	0.003	0.002	0.000	-0.146	-0.124	-0.240
0	1	0.007	0.000	0.002	0.124	-0.002	0.096
1	1	0.000	0.007	-0.003	-0.240	-0.096	-0.140

Table 2: All the possible overlaps ($\alpha_{\ell_1, n_1, \ell_2, n_2}$) between the confined states for $R = 50\text{nm}$ and $\theta_R = 0$.

$\ell_1 \backslash \ell_2$		n_2		0		1	2
		-2	-1	-1	1	1	1
-2	-1	0.398	0.648	0.482	-0.144	0.407	0.279
	1	-0.052	0.094	-0.078	-0.066	-0.170	-0.152
-1	-1	0.623	0.918	0.401	-0.169	0.136	0.010
	1	0.010	0.136	-0.169	-0.401	-0.918	-0.623
0	1	-0.152	-0.170	-0.066	0.078	-0.094	0.052
1	1	0.279	0.407	-0.144	-0.482	-0.648	-0.398

Table 3: All the possible tunnelings ($\gamma_{\ell_1, n_1, \ell_2, n_2}$) in meV between the confined states for $R = 50\text{nm}$ and $\theta_R = 0$.

Continuing with the Coulomb interaction, we must note that, in the case considered, the electron density only depends on the absolute value of the angular quantum number, and, as a consequence, so does the Coulomb potential they create. We plot the different obtained electron densities and their corresponding Coulomb potentials for the different ℓ in Figs. 9.

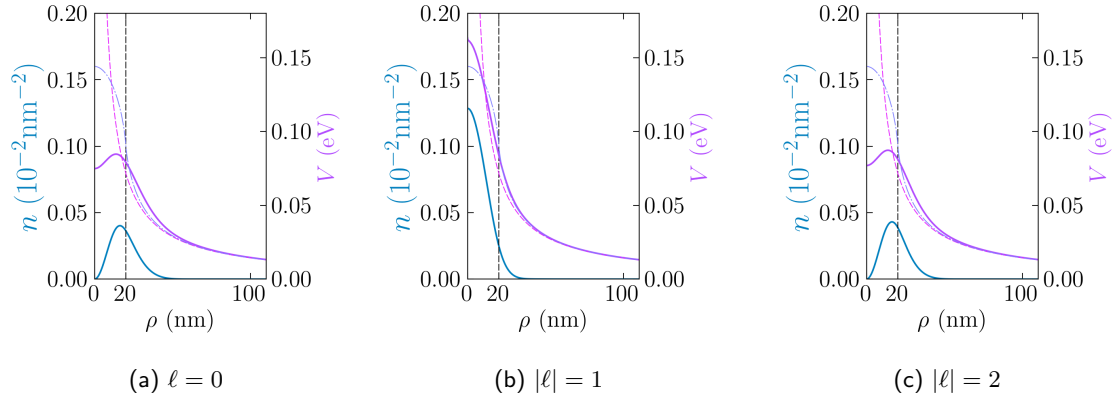


Figure 9: Total electron density n_ℓ (blue) and the corresponding Coulomb potential (purple), as a function of the radial distance ρ for the confined states. The pink dashed line represents e^2/ρ and the purple dash-dotted represents the coulomb potential for a uniformly charged disk of radius 20nm with total charge e , which serve as a reference for the potential.

Finally, the near-site Coulomb interaction between two QDs with $\ell = 0$ is plotted in Fig. 10.

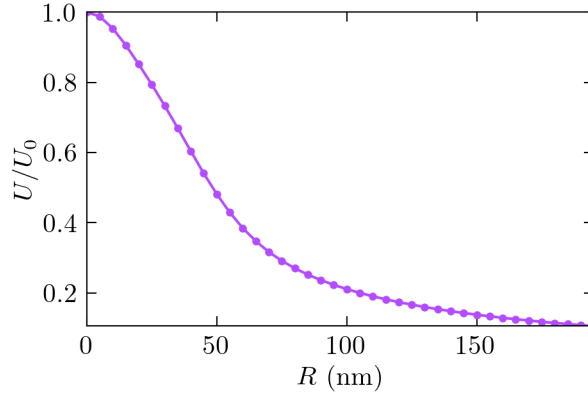


Figure 10: Near site coulomb interaction for $\ell = 0$ divided by the on-site Coulomb interaction ($U_0 = 0.0354$ eV) as a function of the distance between sites R .

Summing up, in this section we have calculated some examples of the Hubbard parameters. Besides, the routines are flexible and can perform such calculations for any obtained confined state. For more information, see the explanations in the supplementary material 5.

3.3 Electronic band-structure of bilayer graphene under a periodic potential

We lastly study the response of BLG under a periodic potential, since our goal is to construct and study an array of quantum dots under a superlattice potential. Therefore, the average potential and the interlayer asymmetry will satisfy

$$V(\mathbf{r} + \mathbf{R}) = V(\mathbf{r}), \quad (36)$$

$$\Delta(\mathbf{r} + \mathbf{R}) = \Delta(\mathbf{r}), \quad (37)$$

where $\mathbf{R} = n_1 \mathbf{a}_1 + n_2 \mathbf{a}_2$ is the lattice vector that defines the periodicity of the potential, given that $n_1, n_2 \in \mathbb{Z}$, and that \mathbf{a}_1 and \mathbf{a}_2 are the primitive lattice vectors. We know from

Bloch's theorem that the wavefunctions that solve Schrödinger's equation in such a periodic potential can be written as

$$\psi_{\mathbf{k},\nu}(\mathbf{r}) = e^{i\mathbf{k}\cdot\mathbf{r}}u_{\mathbf{k},\nu}(\mathbf{r}), \quad (38)$$

where base functions u have the same periodicity as the potential ($u_{\mathbf{k},\nu}(\mathbf{r}) = u_{\mathbf{k},\nu}(\mathbf{r} + \mathbf{R})$), ν is the band index and \mathbf{k} is the crystal momentum of the superlattice.

Considering BLG, we have to note that our base functions will be spinors. Taking this into account, we choose an orthonormal base that respects Eq. 38, which reads

$$\psi_{\mathbf{k},\mathbf{G},\lambda}(\mathbf{r}) = \langle \mathbf{r} | \mathbf{k}, \mathbf{G}, \lambda \rangle = \frac{1}{\sqrt{S}} e^{i(\mathbf{k}+\mathbf{G})\cdot\mathbf{r}} \chi_{\lambda} \quad (39)$$

where S is the total area, $\lambda = \pm 1$ is the layer number and the χ_{\pm} are a basis of the layer subspace

$$\chi_{+} = \begin{pmatrix} 1 \\ 0 \end{pmatrix}, \quad \chi_{-} = \begin{pmatrix} 0 \\ 1 \end{pmatrix}. \quad (40)$$

Taking the Hamiltonian for BLG under an arbitrary potential 14 and considering the case where this potential is periodic, we can construct that Hamiltonian in the described basis. The components for any $\mathbf{k} \in B.Z$ ³ are

$$\begin{aligned} \langle \mathbf{k}, \mathbf{G}, \lambda | \mathcal{H} | \mathbf{k}, \mathbf{G}', \lambda' \rangle = & -\alpha \delta_{\mathbf{G}\mathbf{G}'} \chi_{\lambda}^{\dagger} \begin{pmatrix} 0 & [k_x + G_x - i(k_y + G_y)]^2 \\ [k_x + G_x + i(k_y + G_y)]^2 & 0 \end{pmatrix} \chi_{\lambda'} \\ & + \chi_{\lambda}^{\dagger} \begin{pmatrix} V_{\mathbf{G}'-\mathbf{G}} + \frac{\Delta_{\mathbf{G}'-\mathbf{G}}}{2} & 0 \\ 0 & V_{\mathbf{G}'-\mathbf{G}} - \frac{\Delta_{\mathbf{G}'-\mathbf{G}}}{2} \end{pmatrix} \chi_{\lambda'}, \end{aligned} \quad (41)$$

where $V_{\mathbf{G}}$ and $\Delta_{\mathbf{G}}$ are the Fourier components of the average potential and the interlayer asymmetry in the reciprocal lattice point \mathbf{G} , respectively.

Using Python package `pybandstructure` [Torb, NTK⁺20] we can implement the periodic Hamiltonian described in Eq. 41 and therefore calculate the band structure of BLG under any induced superlattice.

3.3.1 Electronic band-structure of a square array of quantum dots in bilayer graphene

We will study a superlattice potential that creates arrays of quantum dots. Thus, we will have a periodic repetition of the potential generating a single quantum dot described in Eqs. 24 and 25, i.e.,

$$V(\mathbf{r}) = \sum_{\mathbf{R}} V_{\text{dot}}(|\mathbf{r} - \mathbf{R}|) + V_{\text{out}}, \quad (42)$$

$$\Delta(\mathbf{r}) = \sum_{\mathbf{R}} \Delta_{\text{dot}}(|\mathbf{r} - \mathbf{R}|) + \Delta_{\text{out}}. \quad (43)$$

For this concrete example, we choose the same dot potentials (V_{dot} and Δ_{dot}) used in section 3.1.1 repeated in the form of a square lattice, with primitive lattice vectors $\mathbf{a}_1 = a(1, 0)$ and $\mathbf{a}_2 = a(0, 1)$, where a is the lattice constant.

We obtain the total Hamiltonian by inserting in Eq. 41 the Fourier components of the described potential. Remember that the Fourier components are obtained at all the considered points in the reciprocal lattice of the square superlattice. As $V_{\text{dot}} = 0$, $V_{\mathbf{G}} =$

³1st Brillouin zone

$0 \forall \mathbf{G}$. Thus, we only need to calculate the Fourier components $\Delta_{\mathbf{G}}$. Due to the symmetry of the system, we perform the correspondent integral of the Fourier transform only in the unit cell (u.c.), which reads

$$\begin{aligned} \Delta_{\mathbf{G}} &= \int_{u.c.} \frac{d^2\mathbf{r}}{S_{u.c.}} \Delta(\mathbf{r}) e^{-i\mathbf{G}\cdot\mathbf{r}} = \Delta_{out} \delta_{\mathbf{G},0} - \int_0^\infty \rho d\rho \int_{-\pi}^{+\pi} d\theta \frac{\Delta_{well}}{S_{u.c.}} \theta(\rho_0 - \rho) e^{-iG\rho \cos\theta} \\ &= \Delta_{out} \delta_{\mathbf{G},0} - \frac{\Delta_{well}}{S_{u.c.}} \frac{2\pi\rho_0}{G} J_1(G\rho_0), \end{aligned} \quad (44)$$

where $S_{u.c.}$ is the area of the unit cell and the $J_\alpha(x)$ are the Bessel functions of the first kind.

We calculate the band structure and the Density of States (DoS) for different values of a . We chose the values of $a = 50\text{nm}$ and $a = 150\text{nm}$, expecting strong and null interactions between sites, respectively. We plot the results in Figs. 11. For more details on the calculations, see the supplementary material 5.

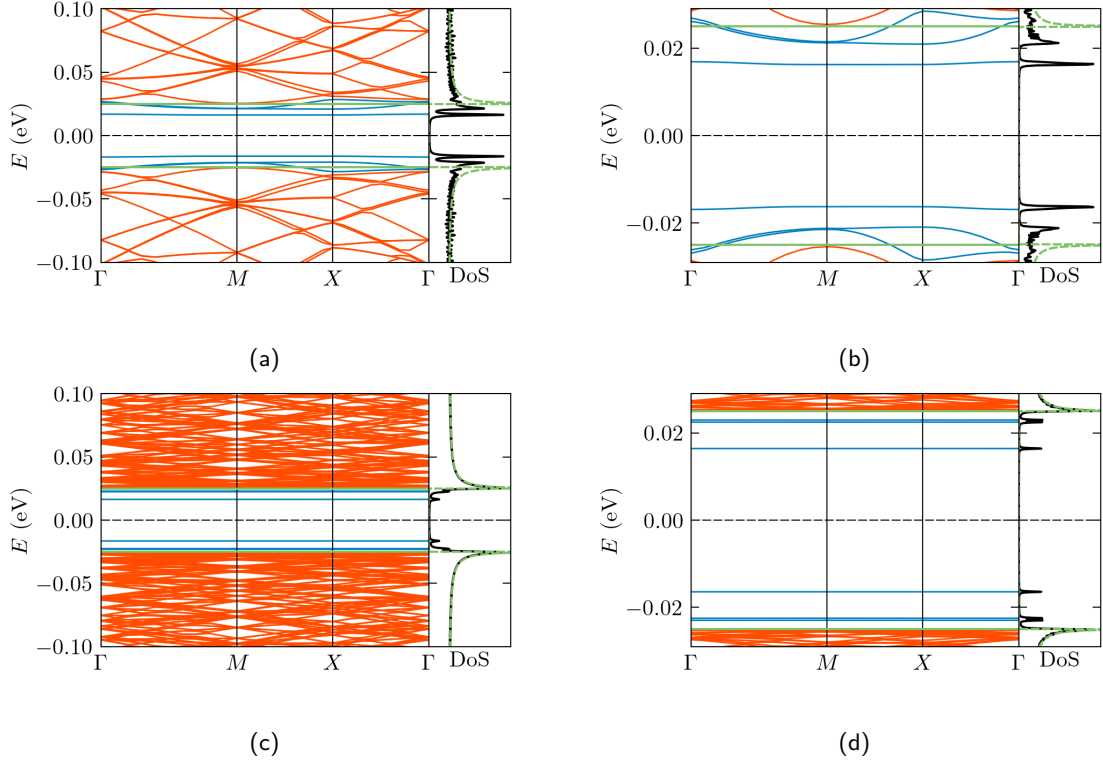


Figure 11: Band structure between high symmetry points Γ , M , X and DoS in different energetic ranges for a square lattice of Δ_{dot} with lattice constant $a = 50\text{nm}$ (**a**, **b**) and $a=150\text{nm}$ (**c**, **d**). The confined bands are plotted in blue, and the non-confined ones in red. The green lines in the band structure represent the outer interlayer asymmetry $\pm\Delta_{out}/2$ and the dashed green line represents the DoS of BLG with interlayer asymmetry Δ_{out} .

We clearly see that in the more spaced case ($a = 150\text{nm}$), we recover the energy levels obtained for a single dot, as we can easily ascertain going back to Fig. 6. Thus, we have no interaction between different dots, as we could predict from the interaction parameters calculated in section 3.2.1. Alternatively, in the case with a superlattice constant of $a = 50\text{nm}$, as the quantum dots interact, the band structure bends.

4 Conclusions

In this work, we have made the first main steps to characterize electrostatically-defined quantum dots in bilayer graphene.

We have started by studying a single quantum dot. In order to do that, two different parts of the problem have been examined and implemented numerically. On the one hand, we have obtained the first approach of the electrostatic potential and displacement field inside the device. As free charges appear in BLG and that provokes a change in the initially solved problem, the subsequent step is to take into account the response of charges in BLG by recursively solving the problem. On the other hand, we have solved the Schrödinger equation in BLG for an arbitrary central electrostatic potential, being capable of obtaining the eigenenergies and eigenfunctions of the confined states, which are the quantum dots to be studied. We remark here that we have proposed how to implement iterative solving of the electrostatic problem considering the response of BLG. Nonetheless, we have made the approach to the response by considering the calculations done for BLG under a homogeneous potential. One could also calculate a more realistic response of BLG (using the programs implemented in section 3) to the potential calculated in section 2, and obtain the free charge density in each layer from the resultant wavefunctions. Nevertheless, we consider that too computationally demanding, as we should also solve the Schrödinger equation for each iteration.

After having studied single dots, we computed the interactions between different dots, calculating the Hubbard parameters describing an array of dots. Moreover, the band structure of BLG under a superlattice potential has been obtained. To validate the equivalence between both approaches, the results can be compared by obtaining the TB Hamiltonian of the system with the calculated TB parameters and obtaining its band structure.

Summing up, we have provided the numerical and computational tools to characterize arrays of gate-defined quantum dots induced in BLG. With them, we are capable to obtain the parameters of the Hubbard model Hamiltonian we are modeling with this analog quantum simulator. In this way, we have built a flexible platform to test possible devices, as we are able to easily change the parameters that define the dot, such as the separation between dots in the superlattice or the size of the hole in the patterned gate. This enables us to obtain a device with a desired response more easily. Moreover, these theoretical simulations serve as theoretical backups to compare with the experimental results. Furthermore, even if the calculations have been done only for BLG, the calculations are easily implementable for other similar materials, such as graphene or Transition Metal Dichalcogenides (TMDs). Last but not least, remark that the central potentials implemented can be used to study other wave equations in 2D with radial symmetry, such as the equations that arise when calculating the binding energy of excitons in two-dimensional materials.

5 Supplementary material

All the calculations done have been implemented in Python and put together in the package `cylindrical_waveequations` [NT] released under public license GNU gpl3. Moreover, all the examples done in this work, with detailed information for each step, can be found in some notebooks stored in https://github.com/saru1799/supplementary_mat_qdblq. All the modules are provided there too, so it is not necessary to directly install the package.

Acknowledgements

First and foremost, I would like to extend my deepest thanks to Iacopo Torre for guiding me through this work. It has been a pleasure to work hand to hand with you and learn from you. I would also like to extend my heartfelt appreciation to Frank Koppens, for trusting me to pursue this task by giving me the opportunity to become part of the QNOE family for these last months, and to all the people in ICFO that make research quite “easier” in some sense. Furthermore, I would like to express my gratitude to the entire QNOE, who have contributed to my growth as a researcher and have made coming to ICFO a lot easier. In special, thanks to all the friends I have done because of ICFO, you have also become what you call “my *real* friends”.

I would also like to thank the coordinating team of the Master’s in Quantum Science and Technology of Barcelona for their confidence and for all the efforts to give us opportunities to grow as a scientist in such a great program.

Continuing with my friends, the ones that deserve my full gratitude are those who have made Barcelona feel a lot more like home: my master partners. Studying is a lot easier when surrounded by wonderful people like you (and when having a rural house to look forward to). In special, thanks to our peculiar “Minister Council” because each of you has stolen a piece of my heart: Dani, for being the sweetest Canarian I could have found and always giving me the confidence that you will be there for me (I will miss you too much); Enrique, for handing me a list of places to eat every time that was needed and being the most Sevillian person I know; Eric, for being the best person I could have sitting next to me in class and having always my back; Hector, for being the person that has endured me the most (principally time), it is a pleasure to share sorrows as long as it is with you; Jordi, for being such truthful to yourself and always being in for a long walk with a profound conversation; Jorge, you deserve the title of the funniest person in the class and I glad that I will continue having that escape route near me for 4 years more; Patri, for having such a pure heart and because being with you feels like having a lemon ice cream in Barcelona in summer; and to Teo, for all the coffees under the sun, even if you are the one that feels as ray of sunshine in a cold winter day and makes everything seem a little bit easier.

The other two people from the master’s that deserve my total gratitude are Ameer and Diana. Ameer, I am so grateful that we have become closer, it is always great to have a person that has such good taste and that draws a smile on my face as easily as you do; this world would be lots better with more people like you. And Diana, because your house has become my house, but especially *you* feel like home. You really make my Mondays and weeks in general easier. Moreover, I have also had the pleasure to be at ICFO with some of the master friends that have accompanied me these months. Thanks for all the “ICFO esmorzar” to Elsa and Vera, and also to Laia for always receiving me with a smile in her “office”. Last but not least, to Alberto and Paula, I am glad that I have gotten to know you and have you near me these months, you make me look forward to Thursday every week.

I would also like to thank all the people that have given me the motivation to get to be where I am, always being there to support me and believe in me. First, to all of the friends I made in my bachelor’s. In particular to Borja, Idoia, Iker, Manex A., Manex I., Marina, Mireia, Naroa and Sara. Thanks to you I am the person I am today and it has been a pleasure to spend 5 of the best years of my life with you. In special, I would like to thank Iker for always being there; and Manex A., for teaching me lessons that go way beyond physics and that really matter in life. I am glad to have spent the last three years of the university so close to you both. And, of course, I do not forget my friends in Elgoibar and

Villaquejida. None of this would be possible if I did not know that, even in the distance, you would be there for me.

Finally, I am deeply indebted to my family for their encouragement, understanding, and love. It has not been an easy year, but I will always feel lucky of having them.

In conclusion, the successful completion of this master's thesis would not have been possible without the guidance, support, and contributions of the individuals mentioned above. I am truly grateful for the people in my life, none of this would be possible without them.

Bibliography

- [ABC⁺21] Ehud Altman, Kenneth R. Brown, Giuseppe Carleo, Lincoln D. Carr, Eugene Demler, Cheng Chin, Brian DeMarco, Sophia E. Economou, Mark A. Eriksson, Kai-Mei C. Fu, Markus Greiner, Kaden R.A. Hazzard, Randall G. Hulet, Alicia J. Kollár, Benjamin L. Lev, Mikhail D. Lukin, Ruichao Ma, Xiao Mi, Shashank Misra, Christopher Monroe, Kater Murch, Zaira Nazario, Kang-Kuen Ni, Andrew C. Potter, Pedram Roushan, Mark Saffman, Monika Schleier-Smith, Irfan Siddiqi, Raymond Simmonds, Meenakshi Singh, I.B. Spielman, Kristan Temme, David S. Weiss, Jelena Vučković, Vladan Vuletić, Jun Ye, and Martin Zwierlein. Quantum simulators: Architectures and opportunities. *PRX Quantum*, 2:017003, Feb 2021.
- [ABH⁺15] Martin Alnæs, Jan Blechta, Johan Hake, August Johansson, Benjamin Kehlet, Anders Logg, Chris Richardson, Johannes Ring, Marie Rognes, and Garth Wells. The FEniCS project version 1.5. 3, 01 2015.
- [Ash76] Neil W. Ashcroft. *Solid state physics*. Holt, Rinehart and Winston, 1976.
- [Aue98] Assa Auerbach. *Interacting Electrons and Quantum Magnetism (Graduate Texts in Contemporary Physics)*. Springer, 1998.
- [BFE⁺18] L. Banszerus, B. Frohn, A. Epping, D. Neumaier, K. Watanabe, T. Taniguchi, and C. Stampfer. Gate-defined electron-hole double dots in bilayer graphene. *Nano Letters*, 18(8):4785–4790, June 2018.
- [BHH⁺22] David Barcons, Hanan Herzig, Rebecca Hoffmann, Iacopo Torre, Hitesh Agarwal, Roshan Krishna Kumar, Lorenzo Vistoli, Takashi Taniguchi, Kenji Watanabe, Adrian Bachtold, and Frank H. L. Koppens. Engineering high quality graphene superlattices via ion milled ultra-thin etching masks. *Nature Communications*, 13(1), November 2022.
- [BMH⁺23] L. Banszerus, S. Möller, K. Hecker, E. Icking, K. Watanabe, T. Taniguchi, F. Hassler, C. Volk, and C. Stampfer. Particle-hole symmetry protects spin-valley blockade in graphene quantum dots. *Nature*, 618(7963):51–56, May 2023.
- [BN09] Iulia Buluta and Franco Nori. Quantum Simulators. *Science*, 326(5949):108–111, October 2009.
- [BR12] R. Blatt and C. F. Roos. Quantum simulations with trapped ions. *Nature Physics*, 8(4):277–284, April 2012.
- [BV13] Pierre Barthelemy and Lieven M. K. Vandersypen. Quantum dot systems: a versatile platform for quantum simulations. *Annalen der Physik*, 525(10-11):808–826, September 2013.
- [Cho23] Jae-yoon Choi. Quantum simulations with ultracold atoms in optical lattices: past, present and future. *Journal of the Korean Physical Society*, 82(9):875–881, March 2023.

- [DYM⁺10] C. R. Dean, A. F. Young, I. Meric, C. Lee, L. Wang, S. Sorgenfrei, K. Watanabe, T. Taniguchi, P. Kim, K. L. Shepard, and J. Hone. Boron nitride substrates for high-quality graphene electronics. *Nature Nanotechnology*, 5(10):722–726, August 2010.
- [EPP⁺18] Marius Eich, Riccardo Pisoni, Alessia Pally, Hiske Overweg, Annika Kurzmann, Yongjin Lee, Peter Rickhaus, Kenji Watanabe, Takashi Taniguchi, Klaus Ensslin, and Thomas Ihn. Coupled Quantum Dots in Bilayer Graphene. *Nano Letters*, 18(8):5042–5048, August 2018.
- [Fey82] Richard P. Feynman. Simulating physics with computers. *International Journal of Theoretical Physics*, 21(6-7):467–488, June 1982.
- [GAN14] I. M. Georgescu, S. Ashhab, and Franco Nori. Quantum simulation. *Reviews of Modern Physics*, 86(1):153–185, March 2014.
- [GB17] Christian Gross and Immanuel Bloch. Quantum simulations with ultracold atoms in optical lattices. *Science*, 357(6355):995–1001, September 2017.
- [GDA⁺23] Sayed Ali Akbar Ghorashi, Aaron Dunbrack, Ahmed Abouelkomsan, Jiacheng Sun, Xu Du, and Jennifer Cano. Topological and stacked flat bands in bilayer graphene with a superlattice potential. *Physical Review Letters*, 130(19):196201, May 2023.
- [GR09] Christophe Geuzaine and Jean-François Remacle. Gmsh: A 3-D finite element mesh generator with built-in pre- and post-processing facilities. *International Journal for Numerical Methods in Engineering*, 79(11):1309–1331, May 2009.
- [HLC⁺20] Robin Huber, Ming-Hao Liu, Szu-Chao Chen, Martin Drienovsky, Andreas Sandner, Kenji Watanabe, Takashi Taniguchi, Klaus Richter, Dieter Weiss, and Jonathan Eroms. Gate-tunable two-dimensional superlattices in graphene. *Nano Letters*, 20(11):8046–8052, October 2020.
- [Hub63] J. Hubbard. Electron correlations in narrow energy bands. *Proceedings of the Royal Society of London. Series A. Mathematical and Physical Sciences*, 276(1365):238–257, November 1963.
- [IBW⁺22] Eike Icking, Luca Banszerus, Frederike Wörtche, Frank Volmer, Philipp Schmidt, Corinne Steiner, Stephan Engels, Jonas Hesselmann, Matthias Goldsche, Kenji Watanabe, Takashi Taniguchi, Christian Volk, Bernd Beschoten, and Christoph Stampfer. Transport spectroscopy of ultraclean tunable band gaps in bilayer graphene. *Advanced Electronic Materials*, 8(11):2200510, July 2022.
- [KCX⁺21] Dante M. Kennes, Martin Claassen, Lede Xian, Antoine Georges, Andrew J. Millis, James Hone, Cory R. Dean, D. N. Basov, Abhay N. Pasupathy, and Angel Rubio. Moiré heterostructures as a condensed-matter quantum simulator. *Nature Physics*, 17(2):155–163, February 2021.
- [KS23] Z. E. Krix and O. P. Sushkov. Patterned bilayer graphene as a tunable strongly correlated system. *Physical Review B*, 107(16):165158, April 2023.
- [LM] Hans Petter Langtangen and Kent-Andre Mardal. *Introduction to Numerical Methods for Variational Problems*. Springer.
- [Log12] Anders Logg. *Automated Solution of Differential Equations by the Finite Element Method The FEniCS Book*. Springer Berlin Heidelberg, 2012.
- [Mal78] Pierre F. Maldague. Many-body corrections to the polarizability of the two-dimensional electron gas. *Surface Science*, 73:296–302, May 1978.
- [McC06] Edward McCann. Asymmetry gap in the electronic band structure of bilayer graphene. *Physical Review B*, 74(16):161403, October 2006.

- [MK13] Edward McCann and Mikito Koshino. The electronic properties of bilayer graphene. *Reports on Progress in Physics*, 76(5):056503, April 2013.
- [MP08] A. Matulis and F. M. Peeters. Quasibound states of quantum dots in single and bilayer graphene. *Physical Review B*, 77(11):115423, March 2008.
- [NT] Sara Navarro and Iacopo Torre. cylindrical_waveequations.
- [NTK⁺20] Pietro Novelli, Iacopo Torre, Frank H. L. Koppens, Fabio Taddei, and Marco Polini. Optical and plasmonic properties of twisted bilayer graphene: Impact of interlayer tunneling asymmetry and ground-state charge inhomogeneity. *Physical Review B*, 102(12):125403, September 2020.
- [OBS⁺06] Taisuke Ohta, Aaron Bostwick, Thomas Seyller, Karsten Horn, and Eli Rotenberg. Controlling the electronic structure of bilayer graphene. *Science*, 313(5789):951–954, August 2006.
- [OHL⁺07] Jeroen B. Oostinga, Hubert B. Heersche, Xinglan Liu, Alberto F. Morpurgo, and Lieven M. K. Vandersypen. Gate-induced insulating state in bilayer graphene devices. *Nature Materials*, 7(2):151–157, December 2007.
- [PYS⁺08] Cheol-Hwan Park, Li Yang, Young-Woo Son, Marvin L. Cohen, and Steven G. Louie. New generation of massless dirac fermions in graphene under external periodic potentials. *Physical Review Letters*, 101(12):126804, September 2008.
- [SGW⁺23] Jiacheng Sun, Sayed Ali Akbar Ghorashi, Kenji Watanabe, Takashi Taniguchi, Fernando Camino, Jennifer Cano, and Xu Du. Signature of correlated insulator in electric field controlled superlattice, 2023.
- [SPP⁺16] M. Singh, J. L. Pacheco, D. Perry, E. Garratt, G. Ten Eyck, N. C. Bishop, J. R. Wendt, R. P. Manginell, J. Dominguez, T. Pluym, D. R. Luhman, E. Bielejec, M. P. Lilly, and M. S. Carroll. Electrostatically defined silicon quantum dots with counted antimony donor implants. *Applied Physics Letters*, 108(6):062101, February 2016.
- [TGU⁺12] Leticia Tarruell, Daniel Greif, Thomas Uehlinger, Gregor Jotzu, and Tilman Esslinger. Creating, moving and merging Dirac points with a Fermi gas in a tunable honeycomb lattice. *Nature*, 483(7389):302–305, March 2012.
- [Tora] Iacopo Torre. diffusive_solver.
- [Torb] Iacopo Torre. pybandstructure.
- [Tor20] Iacopo Torre. Diffusive solver: a diffusion-equations solver based on FEniCS, November 2020.
- [vD21] C.J. van Diepen. *Quantum simulation with electron spins in quantum dots*. PhD thesis, 2021.
- [Wal47] P. R. Wallace. The band theory of graphite. *Physical Review*, 71(9):622–634, May 1947.
- [WKF⁺22] Xiqiao Wang, Ehsan Khatami, Fan Fei, Jonathan Wyrick, Pradeep Nambodiri, Ranjit Kashid, Albert F. Rigosi, Garnett Bryant, and Richard Silver. Experimental realization of an extended fermi-hubbard model using a 2D lattice of dopant-based quantum dots. *Nature Communications*, 13(1), November 2022.
- [WMH⁺13] L. Wang, I. Meric, P. Y. Huang, Q. Gao, Y. Gao, H. Tran, T. Taniguchi, K. Watanabe, L. M. Campos, D. A. Muller, J. Guo, P. Kim, J. Hone, K. L. Shepard, and C. R. Dean. One-dimensional electrical contact to a two-dimensional material. *Science*, 342(6158):614–617, November 2013.
- [YPZ⁺11] Kai Yan, Hailin Peng, Yu Zhou, Hui Li, and Zhongfan Liu. Formation of Bilayer Bernal Graphene: Layer-by-Layer Epitaxy via Chemical Vapor Deposition. *Nano Letters*, 11(3):1106–1110, February 2011.

- [YWS11] Shuo Yang, Xin Wang, and S. Das Sarma. Generic hubbard model description of semiconductor quantum-dot spin qubits. *Physical Review B*, 83(16):161301, April 2011.
- [ZHZ11] K. Zou, X. Hong, and J. Zhu. Effective mass of electrons and holes in bilayer graphene: Electron-hole asymmetry and electron-electron interaction. *Physical Review B*, 84(8):085408, August 2011.

A Properties of uniform bilayer graphene

We analyze the properties of bilayer graphene under a homogeneous potential, i.e., constant in the whole BLG plane. This will serve as the first approach to the properties of BLG under an inhomogeneous potential. We know that the general low-energy Hamiltonian describing it is $\mathcal{H}_{0\xi} + \mathcal{H}_{\text{pot}}$, where these 2 Hamiltonians are the ones expressed in Eqs. 11 and 12. As the potential is constant, it will only change the position of the chemical potential with respect to the states. Thus, we consider the case where only an interlayer asymmetry Δ is present, which energetically differentiates between the two layers. This analysis is also the most relevant to the work done. Therefore, setting $V = 0$, the Hamiltonian becomes

$$\mathcal{H}(\mathbf{k}) = \mathcal{H}_0(\mathbf{k}) + \frac{\Delta}{2}\sigma_z = \begin{pmatrix} \frac{\Delta}{2} & -\frac{\hbar^2}{2m}(\boldsymbol{\pi}^\dagger)^2 \\ -\frac{\hbar^2}{2m}\boldsymbol{\pi}^2 & -\frac{\Delta}{2} \end{pmatrix}. \quad (45)$$

The eigenvalues of this Hamiltonian are

$$\epsilon_\nu(\mathbf{k}) = \nu \sqrt{\frac{\hbar^4 k^4}{4m^2} + \frac{\Delta^2}{4}}, \quad (46)$$

and the associated eigenvectors are

$$\mathbf{v}_\nu(\mathbf{k}) = \frac{1}{\sqrt{2N_\nu(k)}} \begin{pmatrix} 1 \\ -\nu e^{2i\theta_{\mathbf{k}}} \sqrt{2N_\nu(k) - 1} \end{pmatrix}, \quad (47)$$

with

$$N_\nu(k) = 1 + \frac{\frac{\Delta^2}{4} - \nu \frac{\Delta}{2} \sqrt{\frac{\hbar^4 k^4}{4m^2} + \frac{\Delta^2}{4}}}{\frac{\hbar^4 k^4}{4m^2}}. \quad (48)$$

Here, $\nu = \pm 1$ (that differentiates between the bands), and $\theta_{\mathbf{k}}$ is the polar angle of the vector \mathbf{k} .

Note that in the case without interlayer asymmetry, Eqs. 46 and 47 reduce to

$$\epsilon_\nu(\mathbf{k}) = \nu \frac{\hbar^2 k^2}{2m}, \quad (49)$$

$$\mathbf{v}_\nu(\mathbf{k}) = \frac{1}{\sqrt{2}} \begin{pmatrix} 1 \\ -\nu e^{2i\theta_{\mathbf{k}}} \end{pmatrix}. \quad (50)$$

In this work, it will be useful to compute the basis $|\ell, \nu, k\rangle$ of any state. This is done from the free particle expansion of the wavefunctions. We know we can express any state as

$$\Psi(\mathbf{r}) = \sum_{\mathbf{k}\nu} \Psi_{\mathbf{k}\nu}(\mathbf{r}) C_\nu(\mathbf{k}) \quad (51)$$

where

$$\Psi_{\mathbf{k}\nu} = \mathbf{v}_\nu \frac{e^{i\mathbf{k}\cdot\mathbf{r}}}{\sqrt{S}}, \quad (52)$$

and the coefficients read

$$C_\nu(\mathbf{k}) = \sum_{\ell=-\infty}^{\infty} e^{i\ell\theta_{\mathbf{k}}} \delta(k - k_0). \quad (53)$$

Inserting the normalization condition $\langle \ell' \nu' k' | \ell \nu k \rangle = \delta_{\ell\ell'} \delta_{\nu\nu'} \delta(k - k')$ and performing the needed integrals leads to the expression

$$\langle \mathbf{r} | \ell \nu k \rangle = \sqrt{\frac{k}{2\pi}} \frac{e^{i\ell\theta}}{\sqrt{2N_\nu(k)}} \left(\nu e^{i\theta} \sqrt{2N_\nu(k) - 1} J_{\ell+1}(kr) \right) \quad (54)$$

Going back to the electronic properties, the density of states (DOS) is

$$\text{DOS}(\epsilon) = g_s g_v \frac{1}{L^2} \sum_{\mathbf{k}, \nu} \delta(\epsilon - \epsilon_\nu(\mathbf{k})) = \begin{cases} \frac{2m}{\pi\hbar^2} \frac{\epsilon}{\sqrt{\epsilon^2 - \frac{\Delta^2}{4}}} & \epsilon > \frac{|\Delta|}{2} \\ 0 & -\frac{|\Delta|}{2} < \epsilon < \frac{|\Delta|}{2} \\ -\frac{2m}{\pi\hbar^2} \frac{\epsilon}{\sqrt{\epsilon^2 - \frac{\Delta^2}{4}}} & \epsilon < -\frac{|\Delta|}{2} \end{cases} = \frac{2m}{\pi\hbar^2} \text{Re} \left\{ \frac{|\epsilon|}{\sqrt{\epsilon^2 - \frac{\Delta^2}{4}}} \right\}. \quad (55)$$

In the DOS we see that the consideration of the nonzero layer asymmetry has opened a region of forbidden energies (a gap) of size Δ . The appearance of this gap in BLG when $\Delta \neq 0$ will be a crucial point of the current work.

For us, it is more interesting to obtain the DOS projected in each layer, which is the projected DOS (PDOS) and will be

$$\text{PDOS}_l(\epsilon) = g_s g_v \sum_{\mathbf{k}, \nu} \delta(\epsilon - \epsilon_\nu(\mathbf{k})) \mathbf{v}_\nu(\mathbf{k})^\dagger P_l \mathbf{v}_\nu(\mathbf{k}) \quad (56)$$

where l is the layer number, having $l = 1$ for the top layer and $l = -1$ for the bottom layer; and P_l is the projector in each of the layers and is defined as $P_l = \frac{1}{2}(\mathbb{1} + l\sigma_z)$. This leads to

$$\text{PDOS}_l(\epsilon, \Delta) = \begin{cases} \frac{m}{\pi\hbar^2} \sqrt{\frac{\epsilon + l\frac{\Delta}{2}}{\epsilon - l\frac{\Delta}{2}}} & \epsilon > \frac{|\Delta|}{2} \\ 0 & -\frac{|\Delta|}{2} < \epsilon < \frac{|\Delta|}{2} \\ \frac{m}{\pi\hbar^2} \sqrt{\frac{\epsilon + l\frac{\Delta}{2}}{\epsilon - l\frac{\Delta}{2}}} & \epsilon < -\frac{|\Delta|}{2} \end{cases} = \frac{m}{\pi\hbar^2} \text{Re} \left\{ \sqrt{\frac{\epsilon + l\frac{\Delta}{2}}{\epsilon - l\frac{\Delta}{2}}} \right\}. \quad (57)$$

In Figs. 12, we plot the DOS and the PDOS for a constant Δ of value $\Delta = 0.1$ eV.

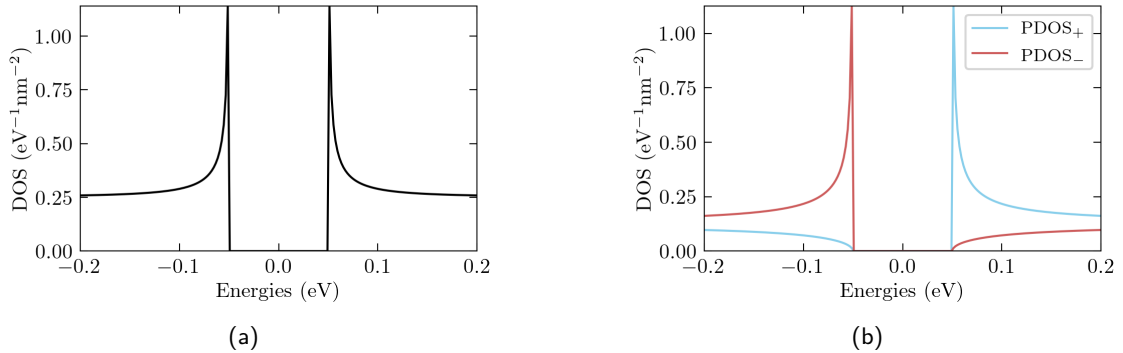


Figure 12: **(a)** DOS and **(b)** projected DOS (blue for the top layer and in red for the bottom layer) as a function of energy for BLG with a constant interlayer asymmetry of $\Delta = 0.1$ eV.

The electronic density in each of the layers n_l is a function of the chemical potential μ , the interlayer asymmetry Δ , and the temperature T . By definition, $n_l = n_{el} - n_{hl}$,

where n_{el} and n_{hl} are the density of electrons and holes in layer l , respectively. Thus, the electronic density in each layer is

$$\begin{aligned}
n_l(\mu, \Delta, \beta) &= \underbrace{\int_0^\infty d\epsilon \text{PDOS}_l(\epsilon, \Delta) f_{FD}(\epsilon, \mu, \beta)}_{n_{el}} - \underbrace{\int_{-\infty}^0 d\epsilon \text{PDOS}_l(\epsilon, \Delta) [1 - f_{FD}(\epsilon, \mu, \beta)]}_{n_{hl}} = \\
&= \frac{m}{\pi \hbar^2} \left(\int_{|\Delta|/2}^\infty d\epsilon \sqrt{\frac{\epsilon + l\frac{\Delta}{2}}{\epsilon - l\frac{\Delta}{2}}} \frac{1}{1 + e^{\beta(\epsilon - \mu)}} - \int_{-\infty}^{-|\Delta|/2} d\epsilon \sqrt{\frac{\epsilon + l\frac{\Delta}{2}}{\epsilon - l\frac{\Delta}{2}}} \frac{1}{1 + e^{-\beta(\epsilon - \mu)}} \right) = \\
&= \frac{m}{\pi \hbar^2} \left(\int_{|\Delta|/2}^\infty d\epsilon \sqrt{\frac{\epsilon + l\frac{\Delta}{2}}{\epsilon - l\frac{\Delta}{2}}} \frac{1}{1 + e^{\beta(\epsilon - \mu)}} - \int_{|\Delta|/2}^\infty d\epsilon \sqrt{\frac{\epsilon - l\frac{\Delta}{2}}{\epsilon + l\frac{\Delta}{2}}} \frac{1}{1 + e^{\beta(\epsilon + \mu)}} \right) = \\
&= \frac{m}{\pi \hbar^2} \left(\int_{|\Delta|/2}^\infty d\epsilon \frac{\epsilon + l\frac{\Delta}{2}}{\sqrt{\epsilon^2 - \frac{\Delta^2}{4}}} \frac{1}{1 + e^{\beta(\epsilon - \mu)}} - \int_{|\Delta|/2}^\infty d\epsilon \frac{\epsilon - l\frac{\Delta}{2}}{\sqrt{\epsilon^2 - \frac{\Delta^2}{4}}} \frac{1}{1 + e^{\beta(\epsilon + \mu)}} \right). \tag{58}
\end{aligned}$$

In the last equation, $f_{FD}(\epsilon, \mu, \beta) = [1 + e^{\beta(\epsilon - \mu)}]^{-1}$ is the Fermi-Dirac distribution function and $\beta = \frac{1}{k_B T}$ where k_B is Boltzmann's constant. These integrals can be solved analytically at zero temperature ($\beta \rightarrow +\infty$) using the identity $[1 + e^{\beta x}]^{-1} \xrightarrow{\beta \rightarrow \infty} \theta(-x)$. Thus Eq. 58 at $T = 0$ becomes

$$n_l(\mu, \Delta, \infty) = \frac{m}{\pi \hbar^2} \left(\int_{|\Delta|/2}^\infty d\epsilon \frac{\epsilon + l\frac{\Delta}{2}}{\sqrt{\epsilon^2 - \frac{\Delta^2}{4}}} \theta(\mu - \epsilon) - \int_{|\Delta|/2}^\infty d\epsilon \frac{\epsilon - l\frac{\Delta}{2}}{\sqrt{\epsilon^2 - \frac{\Delta^2}{4}}} \theta(-\mu - \epsilon) \right). \tag{59}$$

When μ lies inside the gap ($|\mu| < \frac{|\Delta|}{2}$), both integrals in Eq. 59 vanish. When $\mu > \frac{|\Delta|}{2}$ only the first integral, corresponding to a density of electrons, will have a non-zero value. This leads to

$$\begin{aligned}
n_l(\mu, \Delta, \beta = \infty) &\xrightarrow{\mu > |\Delta|/2} \frac{m}{\pi \hbar^2} \int_{|\Delta|/2}^\mu d\epsilon \frac{\epsilon + l\frac{\Delta}{2}}{\sqrt{\epsilon^2 + \frac{\Delta^2}{4}}} = \\
&\frac{m}{\pi \hbar^2} \left[\sqrt{\mu^2 - \frac{\Delta^2}{4}} + l\frac{\Delta}{2} \operatorname{arcosh} \left(\frac{2\mu}{|\Delta|} \right) \right], \tag{60}
\end{aligned}$$

where for $\Delta = 0$ the second part vanishes. Similarly, for $\mu < -\frac{|\Delta|}{2}$, only the second integral (corresponding to the density of holes) contributes, yielding

$$\begin{aligned}
n_l(\mu, \Delta, \beta = \infty) &\xrightarrow{-\mu > |\Delta|/2} -\frac{m}{\pi \hbar^2} \int_{|\Delta|/2}^{-\mu} d\epsilon \frac{\epsilon - l\frac{\Delta}{2}}{\sqrt{\epsilon^2 + \frac{\Delta^2}{4}}} = \\
&\frac{m}{\pi \hbar^2} \left[-\sqrt{\mu^2 - \frac{\Delta^2}{4}} + l\frac{\Delta}{2} \operatorname{arcosh} \left(\frac{-2\mu}{|\Delta|} \right) \right]. \tag{61}
\end{aligned}$$

Putting the three cases together, we obtain

$$n_l(\mu, \Delta, \beta = \infty) = \frac{m}{\pi \hbar^2} \left[\operatorname{sgn}(\mu) \sqrt{\mu^2 - \frac{\Delta^2}{4}} + l\frac{\Delta}{2} \operatorname{arcosh} \left(\frac{2|\mu|}{|\Delta|} \right) \right] \theta(2|\mu| - |\Delta|) \tag{62}$$

This allows us to calculate the total charge density $\varrho = -e(n_+ + n_-)$ and the polarization density $P_z = -et_z(n_+ - n_-)/2$, where t_z is the distance between the layers and e is the unit charge. This yields to

$$\varrho(\mu, \Delta, \beta = \infty) = -e \frac{2m}{\pi \hbar^2} \operatorname{sgn}(\mu) \operatorname{Re} \left\{ \sqrt{\mu^2 - \frac{\Delta^2}{4}} \right\} \quad (63)$$

and

$$P_z(\mu, \Delta, \beta = \infty) = -et_z \frac{m}{\pi \hbar^2} \Delta \operatorname{Re} \left\{ \operatorname{arcosh} \left(\frac{2|\mu|}{|\Delta|} \right) \right\} \quad (64)$$

We plot both $\varrho(\mu)$ and P_z for the previous example of $\Delta = 0.1$ eV in Figs.

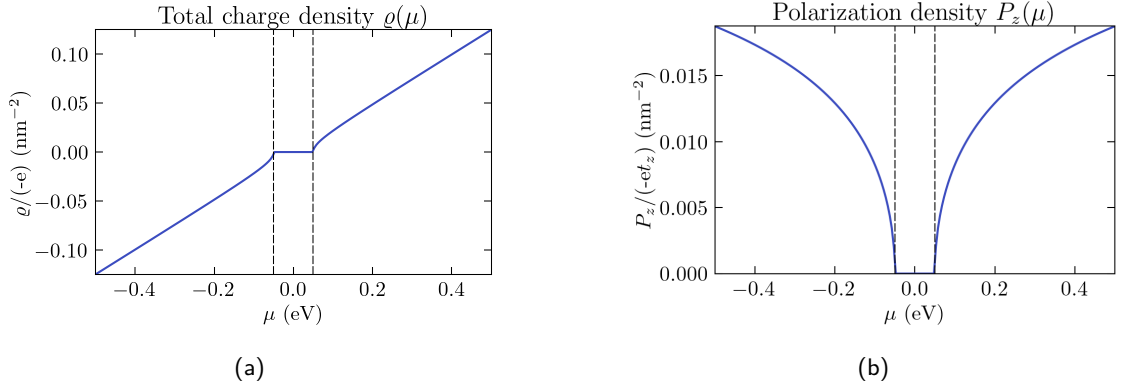


Figure 13: **(a)** Total charge density and **(b)** polarization energy as a function of the chemical potential at $T = 0$ for BLG with a constant interlayer asymmetry of $\Delta = 0.1$ eV. The limits of the gap $\frac{\Delta}{2}$ are marked in dashed lines.

We can calculate n_l at finite temperature using the following identity, known as Maldague's integral [Mal78]:

$$\frac{1}{1 + e^x} = \int_{-\infty}^{\infty} \frac{\theta(y - x)}{4 \cosh^2 \frac{y}{2}} dy, \quad (65)$$

which allows us to express the finite temperature quantities as a rapidly convergent integral involving the corresponding quantities at zero temperature. For the electronic density, we get

$$\begin{aligned} n_l(\mu, \Delta, \beta) &= \frac{m}{\pi \hbar^2} \left(\int_{\frac{|\Delta|}{2}}^{\infty} d\epsilon \frac{\epsilon + l\frac{\Delta}{2}}{\sqrt{\epsilon^2 - \frac{\Delta^2}{4}}} \frac{1}{1 + e^{\beta(\epsilon - \mu)}} - \int_{\frac{|\Delta|}{2}}^{\infty} d\epsilon \frac{\epsilon - l\frac{\Delta}{2}}{\sqrt{\epsilon^2 - \frac{\Delta^2}{4}}} \frac{1}{1 + e^{\beta(\epsilon + \mu)}} \right) = \\ &= \frac{m}{\pi \hbar^2} \left\{ \int_{\beta(\frac{|\Delta|}{2} - \mu)}^{\infty} dy \frac{1}{4 \cosh^2 \frac{y}{2}} \left[\sqrt{\left(\frac{y}{\beta} + \mu\right)^2 - \frac{\Delta^2}{4}} + l\frac{\Delta}{2} \operatorname{arcosh} \left(\frac{2\left|\frac{y}{\beta} + \mu\right|}{|\Delta|} \right) \right] \right. \\ &\quad \left. - \int_{\beta(\frac{|\Delta|}{2} + \mu)}^{\infty} dy \frac{1}{4 \cosh^2 \frac{y}{2}} \left[\sqrt{\left(\frac{y}{\beta} - \mu\right)^2 - \frac{\Delta^2}{4}} - l\frac{\Delta}{2} \operatorname{arcosh} \left(\frac{2\left|\frac{y}{\beta} - \mu\right|}{|\Delta|} \right) \right] \right\} = \\ &= \int_{-\infty}^{\infty} dy \frac{1}{4 \cosh^2 \left(\frac{y}{2}\right)} n_l \left(\mu + \frac{y}{\beta}, \Delta, \beta = \infty \right). \end{aligned} \quad (66)$$

As we did for the DOS and the PDOS, we obtain the numerical calculation for the electronic densities in each layer for $\Delta = 0.1$ eV, shown in Figs. 14.

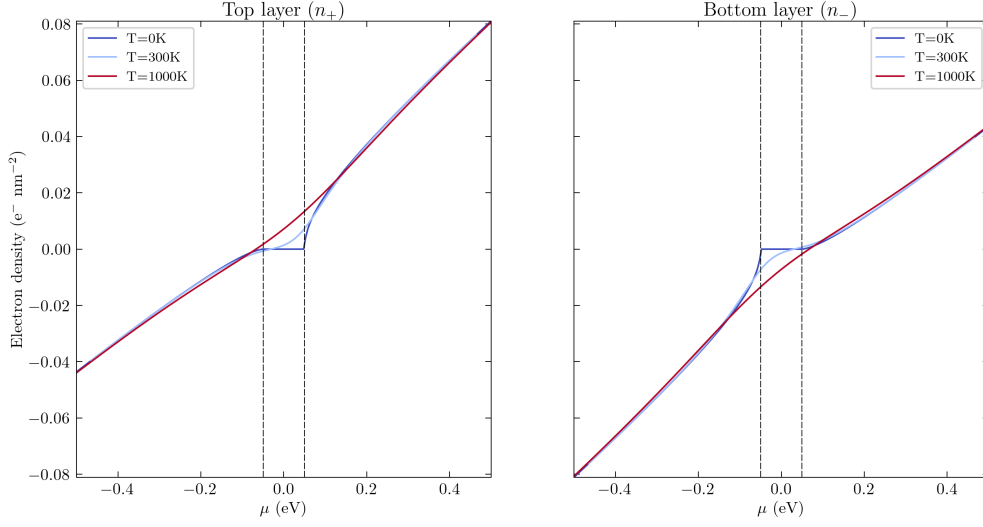


Figure 14: Electronic density in the top (n_+) and bottom (n_-) layers as a function of the chemical potential ν for different temperatures and a fixed interlayer asymmetry of $\Delta = 0.1\text{eV}$. The dashed lines correspond to $\mu = \pm \frac{\Delta}{2}$

Thus, the total charge density at finite temperature reads

$$\begin{aligned} \varrho(\mu, \Delta, \beta) = & -\frac{em}{\pi\hbar^2} \left\{ \int_{\beta(\frac{|\Delta|}{2}-\mu)}^{\infty} dy \frac{1}{2 \cosh^2 \frac{y}{2}} \sqrt{\left(\frac{y}{\beta} + \mu\right)^2 - \frac{\Delta^2}{4}} \right. \\ & \left. - \int_{\beta(\frac{|\Delta|}{2}+\mu)}^{\infty} dy \frac{1}{2 \cosh^2 \frac{y}{2}} \sqrt{\left(\frac{y}{\beta} - \mu\right)^2 - \frac{\Delta^2}{4}} \right\} = \\ & \int_{-\infty}^{\infty} dy \frac{1}{4 \cosh^2(\frac{y}{2})} \varrho\left(\mu + \frac{y}{\beta}, \Delta, \beta = \infty\right); \end{aligned} \quad (67)$$

and for the polarization density, we have

$$\begin{aligned} P_z(\mu, \Delta, \beta) = & -\frac{et_z m}{\pi\hbar^2} \left\{ \int_{\beta(\frac{|\Delta|}{2}-\mu)}^{\infty} dy \frac{\Delta}{8 \cosh^2 \frac{y}{2}} \text{Re} \left\{ \text{arcosh} \left(\frac{2\left(\frac{y}{\beta} + \mu\right)}{|\Delta|} \right) \right\} \right. \\ & \left. + \int_{\beta(\frac{|\Delta|}{2}+\mu)}^{\infty} dy \frac{\Delta}{8 \cosh^2 \frac{y}{2}} \text{Re} \left\{ \text{arcosh} \left(\frac{2\left(\frac{y}{\beta} - \mu\right)}{|\Delta|} \right) \right\} \right\} = \\ & \int_{-\infty}^{\infty} dy \frac{1}{4 \cosh^2(\frac{y}{2})} P_z\left(\mu + \frac{y}{\beta}, \Delta, \beta = \infty\right). \end{aligned} \quad (68)$$

We see that this enables us to get the values for finite temperatures as a function of the expressions for zero temperature.

B Discretization of the eigenvalue/eigenvector equations for bilayer graphene under a radially symmetric potential using the finite element method

Here we solve the system of equations obtained for the radial part of the wavefunctions of BLG under a radial potential, which read

$$\alpha \left[\ddot{u}_{\ell,-}(\rho) + \frac{1+2\ell}{\rho} \dot{u}_{\ell,-}(\rho) + \frac{\ell^2-1}{\rho^2} u_{\ell,-}(\rho) \right] + \left[V(\rho) + \frac{\Delta(\rho)}{2} \right] u_{\ell,+}(\rho) = E u_{\ell,+}(\rho), \quad (69)$$

$$\alpha \left[\ddot{u}_{\ell,+}(\rho) + \frac{1-2\ell}{\rho} \dot{u}_{\ell,+}(\rho) + \frac{\ell^2-1}{\rho^2} u_{\ell,+}(\rho) \right] + \left[V(\rho) - \frac{\Delta(\rho)}{2} \right] u_{\ell,-}(\rho) = E u_{\ell,-}(\rho). \quad (70)$$

We first study the boundary conditions we need to impose and then use the FEM to get the numerical implementation of the problem.

B.1 Obtaining the boundary conditions

In order to discretize the equations, we need the boundary conditions (BC) at the boundaries of the considered coordinate ρ , i.e., at $\rho = 0$ and at $\rho = \rho_{max}$.

We will start with the case $\boldsymbol{\rho} = \mathbf{0}$. Multiplying Eqs. 69 and 70 by ρ^2 and fixing $\rho = 0$ would leave us with:

$$(\ell^2 - 1)u_{\ell,+}(0) = 0, \quad (\ell^2 - 1)u_{\ell,-}(0) = 0. \quad (71)$$

As ℓ is fixed, this distinguishes two different cases, which we will analyze separately: $\ell^2 \neq 1$ and $\ell = \pm 1$.

$\ell^2 \neq 1$

From the Eqs. at $\rho = 0$ written in 71, we see that in this case we must have $u_{\ell,+}(0) = 0$ and $u_{\ell,-}(0) = 0$. Thus, this fixes our boundary conditions.

$\ell = \pm 1$

In this case, we return to Eqs. 69 and 70 and see that the zero order term vanishes. We analyze the equations by expanding $u_{\ell, \pm}$ till the second order. This leaves us with two different cases. For $\ell = 1$, we have that:

$$\dot{u}_{+1,+}(\rho = 0) = 0, \quad u_{+1,-}(\rho = 0) = 0; \quad (72)$$

while for $\ell = -1$:

$$\dot{u}_{-1,-}(\rho = 0) = 0, \quad u_{-1,+}(\rho = 0) = 0. \quad (73)$$

We proceed with the boundary condition at $\boldsymbol{\rho} = \boldsymbol{\rho}_{max}$. As we know the wavefunctions should decay as $\rho \rightarrow \infty$ we just fix $u_{\ell,+}(\rho_{max}) = u_{\ell,-}(\rho_{max}) = 0$ by assuming that the chosen ρ_{max} is large enough.

B.2 Implementing the finite element method

Now we go back again to Eqs. 69 and 70, and rewrite them in a single equation using the spinor of \mathbf{u} , i.e.:

$$\bar{\mathbf{u}}(\rho) = \begin{pmatrix} u^+(\rho) \\ u^-(\rho) \end{pmatrix} \quad (74)$$

Which leads to (with $\epsilon = E/\alpha$):

$$\underbrace{\begin{pmatrix} 0 & 1 \\ 1 & 0 \end{pmatrix}}_{M_1} \ddot{\mathbf{u}}(\rho) + \underbrace{\begin{pmatrix} 0 & \frac{1+2\ell}{\rho} \\ \frac{1-2\ell}{\rho} & 0 \end{pmatrix}}_{M_2} \dot{\mathbf{u}}(\rho) + \underbrace{\begin{pmatrix} V^+(\rho) & \frac{\ell^2-1}{\rho^2} \\ \frac{\ell^2-1}{\rho^2} & V^-(\rho) \end{pmatrix}}_{M_3} \bar{\mathbf{u}} = \epsilon \begin{pmatrix} 1 & 0 \\ 0 & 1 \end{pmatrix} \bar{\mathbf{u}} \quad (75)$$

where

$$\epsilon = \frac{E}{\alpha}, \quad V^+(\rho) = \frac{1}{\alpha} \left(V(\rho) + \frac{\Delta(\rho)}{2} \right), \quad V^-(\rho) = \frac{1}{\alpha} \left(V(\rho) - \frac{\Delta(\rho)}{2} \right). \quad (76)$$

The next step is to find the weak form of eq. 76. If we call $\bar{v}(\rho) \in W$ to our test function (which will be a spinor), this leads to:

$$\int_0^{\rho_{max}} \rho d\rho \bar{v}^\dagger(\rho) [M_1 \ddot{\mathbf{u}}(\rho) + M_2 \dot{\mathbf{u}}(\rho) + M_3 \bar{\mathbf{u}}(\rho) - \epsilon \bar{\mathbf{u}}(\rho)] = 0 \quad (77)$$

To have the same order of derivatives, we use the integration by parts:

$$\int_0^{\rho_{max}} \rho v^\dagger(\rho) M_1 \ddot{\mathbf{u}}(\rho) = \underbrace{\left[r \bar{v}^\dagger(\rho) M_1 \dot{\mathbf{u}}(\rho) \right]_0^{\rho_{max}}}_{=0} - \int_0^{\rho_{max}} d\rho \left(\bar{v}^\dagger(\rho) + \rho \dot{\bar{v}}^\dagger(\rho) \right) M_1 \dot{\mathbf{u}}(\rho) \quad (78)$$

where the first term cancels due to the BC, as we can impose $\bar{v}(0) = \bar{v}(\rho_{max}) = \bar{0}$ [LM]. Thus, this transforms eq. 77 into:

$$\int_0^{\rho_{max}} d\rho \left[\bar{v}^\dagger(\rho) M_1 \dot{\mathbf{u}}(\rho) + \rho \dot{\bar{v}}^\dagger(\rho) M_1 \dot{\mathbf{u}}(\rho) + \rho \bar{v}^\dagger(\rho) M_2 \dot{\mathbf{u}}(\rho) + \rho \bar{v}^\dagger(\rho) M_3 \bar{\mathbf{u}}(\rho) - \epsilon \bar{\mathbf{u}}(\rho) \right] = 0 \quad (79)$$

From this point on, we decide to only consider the case $\ell^2 \neq 1$, as the boundary conditions are simpler and it is valid to understand how to implement the FEM. For $\ell = \pm 1$, only the solutions will be given after.

We choose the space W to be defined as $W \in \text{span}\{\varphi_i\}$. These functions are defined as a function of our discretization. We have already specified that we are solving the problem in $\rho \in [0, \rho_{max}]$ and this space will be divided into N segments, having $h = \frac{\rho_{max}}{N}$. Consequently, and taking into account that our BCs are $\bar{\mathbf{u}}(0) = \bar{\mathbf{u}}(\rho_{max}) = \bar{0}$, we can also choose $\bar{\mathbf{u}} \in W$, if all the functions in W fulfill the BCs. So we choose the φ_i to be:

$$\varphi_i(\rho) = \begin{cases} \frac{\rho}{h} + 1 - i & (i-1)h < \rho < ih \\ -\frac{\rho}{h} + 1 - i & ih < \rho < (i+1)h \\ 0 & \text{otherwise.} \end{cases} \quad (80)$$

Hence, and representing the different layers by $\lambda = +, -$, and $\chi_+ = \begin{pmatrix} 1 \\ 0 \end{pmatrix}$, $\chi_- = \begin{pmatrix} 0 \\ 1 \end{pmatrix}$ we can write:

$$\bar{\mathbf{v}} = \sum_{i,\lambda} \varphi_i \chi_\lambda v_{i,\lambda} \quad \bar{\mathbf{u}} = \sum_{j,\lambda'} \varphi_j \chi_{\lambda'} v_{j,\lambda'} \quad (81)$$

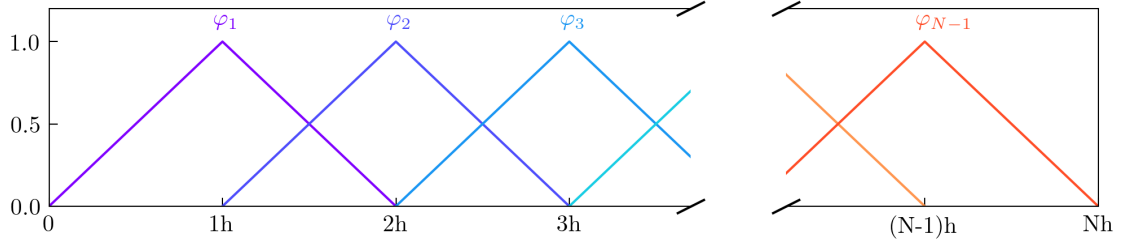


Figure 15: Graphical representation of functions φ_i .

Note that, seeing how we have built the equations, the unknowns $u_{j,\lambda'} \equiv u^+(\rho_j), u^-(\rho_j)$ are the solutions we are looking for. Inserting the power series into eq. 79, leading to

$$\begin{aligned} \sum_{i,j,\lambda,\lambda'} v_{i\lambda} u_{j\lambda'} \int_0^{\rho_{max}} d\rho \left[-\varphi_i \chi_\lambda^\dagger M_1 \dot{\varphi}_j \chi_{\lambda'} - \rho \dot{\varphi}_i \chi_\lambda^\dagger M_1 \dot{\varphi}_j \chi_{\lambda'} + \rho \varphi_i \chi_\lambda^\dagger M_2 \dot{\varphi}_j \chi_{\lambda'} + \rho \varphi_i \chi_\lambda^\dagger M_3 \varphi_j \chi_{\lambda'} \right] = \\ = \epsilon \sum_{i,j,\lambda,\lambda'} v_{i\lambda} u_{j\lambda'} \int_0^{\rho_{max}} \rho d\rho \varphi_i \varphi_j \chi_\lambda^\dagger \chi_{\lambda'} \end{aligned} \quad (82)$$

Note that this equation must be fulfilled for $\forall v_{i\lambda}$ and that $M_1 + \rho M_2 = \frac{2\ell}{\rho} \begin{pmatrix} 0 & 1 \\ -1 & 0 \end{pmatrix} := M_2^\ell$. So, the equation we have is:

$$\begin{aligned} \sum_{i,j,\lambda,\lambda'} u_{j\lambda'} \int_0^{\rho_{max}} d\rho \left[-\rho \dot{\varphi}_i \chi_\lambda^\dagger M_1 \dot{\varphi}_j \chi_{\lambda'} + \rho \varphi_i \chi_\lambda^\dagger M_2^\ell \dot{\varphi}_j \chi_{\lambda'} + \rho \varphi_i \chi_\lambda^\dagger M_3 \varphi_j \chi_{\lambda'} \right] = \\ = \epsilon \sum_{i,j,\lambda,\lambda'} u_{j\lambda'} \int_0^{\rho_{max}} \rho d\rho \varphi_i \varphi_j \chi_\lambda^\dagger \chi_{\lambda'} \end{aligned} \quad (83)$$

This leads to the eigenvalue/eigenvector equations with the form $\bar{M} \cdot \bar{u}_{tot} = \epsilon \bar{W} \cdot \bar{u}_{tot}$, where $\bar{u}_{tot}^\dagger := (u_1, u_2, \dots, u_i, \dots, u_N)$; $u_i := u(\rho_i)$ and we have defined $\rho_i = hi$; $i = 0, 1, 2 \dots N+1$; $\rho_0 = 0$; $\rho_{N+1} = \rho_{max}$. Thus, the matrix M will be defined as

$$M = \frac{\alpha}{h^2} [M^{(K1)} + 2\ell M^{(K2)} + (\ell^2 - 1)M^{(K3)}] + M^{(V)}. \quad (84)$$

All these matrices are symmetric and have the following structure :

$$\left(\begin{array}{c|c|c|c|c} D_1 & P_1 & & & \\ \hline P_1^T & D_2 & P_2 & & \\ \hline & \ddots & \ddots & \ddots & \\ \hline & & P_{N-2}^T & D_{N-1} & P_{N-1} \\ \hline & & & P_{N-1}^T & D_N \end{array} \right) \quad (85)$$

$$D_n^T = D_n \quad (86)$$

We will now define separately all the components (remember that we are in the case $\ell^2 \neq 1$):

Matrix $M^{(K1)}$

$$D_n = \begin{pmatrix} 0 & -2n \\ -2n & 0 \end{pmatrix} \quad P_n = \begin{pmatrix} 0 & n + \frac{1}{2} \\ n + \frac{1}{2} & 0 \end{pmatrix} \quad (87)$$

Matrix $M^{(K2)}$

$$D_n = \begin{pmatrix} 0 & 0 \\ 0 & 0 \end{pmatrix} \quad P_n = \begin{pmatrix} 0 & +\frac{1}{2} \\ -\frac{1}{2} & 0 \end{pmatrix} \quad (88)$$

Matrix $M^{(K3)}$

$$D_n = \begin{pmatrix} 0 & f_n \\ f_n & 0 \end{pmatrix}, \quad P_n = \begin{pmatrix} 0 & g_n \\ g_n & 0 \end{pmatrix}, \quad (89)$$

where

$$f_n = \begin{cases} -2n - (n-1)^2 \ln(1-1/n) + (n+1)^2 \ln(1+1/n) & \text{if } n > 1 \\ -2 + 4 \ln(2) & \text{if } n = 1 \end{cases} \quad (90)$$

$$g_n = \frac{1}{2} + n - n(n+1) \ln(1+1/n) \quad (91)$$

Matrix $M^{(V)}$

We define $V_n^{(\pm)} = V(r_n) \pm \frac{1}{2} \Delta(r_n)$.

$$D_n = \begin{pmatrix} \frac{(5n-2)V_{n-1}^{(+)} + 30nV_n^{(+)} + (5n+2)V_{n+1}^{(+)}}{60} & 0 \\ 0 & \frac{(5n-2)V_{n-1}^{(-)} + 30nV_n^{(-)} + (5n+2)V_{n+1}^{(-)}}{60} \end{pmatrix} \quad (92)$$

$$P_n = \begin{pmatrix} \frac{(5n+2)V_n^{(+)} + (5n+3)V_{n+1}^{(+)}}{60} & 0 \\ 0 & \frac{(5n+2)V_n^{(-)} + (5n+3)V_{n+1}^{(-)}}{60} \end{pmatrix} \quad (93)$$

Matrix W

$$D_n = \begin{pmatrix} \frac{2n}{3} & 0 \\ 0 & \frac{2n}{3} \end{pmatrix}, \quad P_n = \begin{pmatrix} \frac{2n+1}{12} & 0 \\ 0 & \frac{2n+1}{12} \end{pmatrix}. \quad (94)$$

The case $\ell = \pm 1$ is implemented by adding the matrices for $n = 0$ multiplying the term u_{\pm} that does not vanish at $\rho = 0$ (i.e., $u_{\ell,+}$ for $\ell = 1$ and $u_{\ell,-}$ for $\ell = -1$). The rest of the components of the matrices are the same as in the case $\ell^2 \neq 1$. Thus the matrix M will now read

$$M = \frac{\alpha}{h^2} [M^{(K1)} + 2\ell M^{(K2)}] + M^{(V)} \quad (95)$$

being able to write each of the matrices in the way

$$\left(\begin{array}{c|c|c|c|c|c} D_0 & P_0 & & & & \\ \hline P_0^T & D_1 & P_1 & & & \\ \hline & P_1^T & D_2 & P_2 & & \\ \hline & & \ddots & \ddots & \ddots & \\ \hline & & & P_{N-2}^T & D_{N-1} & P_{N-1} \\ \hline & & & & P_{N-1}^T & D_N \end{array} \right), \quad (96)$$

where D_0 is a 1×1 matrix and P_0 a 1×2 one, that depend on the chosen ℓ .

Starting with $\ell = \mathbf{1}$

Matrix $M^{(K1)}$

$$D_0 = (0), \quad P_0 = \left(0 \quad \frac{1}{2}\right). \quad (97)$$

Matrix $M^{(K2)}$

$$D_0 = (0), \quad P_0 = \left(0 \quad \frac{1}{2}\right) \quad (98)$$

Matrix $M^{(V)}$

$$D_0 = \left(\frac{3V_0^{(+)}+2V_1^{(+)}}{60}\right), \quad P_0 = \left(\frac{2V_0^{(+)}+3V_1^{(+)}}{60} \quad 0\right) \quad (99)$$

Matrix W

$$D_0 = \left(\frac{1}{12}\right), \quad P_0 = \left(\frac{1}{12} \quad 0\right). \quad (100)$$

Similarly, in case $\ell = -\mathbf{1}$

Matrix $M^{(K1)}$

$$D_0 = (0), \quad P_0 = \left(\frac{1}{2} \quad 0\right). \quad (101)$$

Matrix $M^{(K2)}$

$$D_0 = (0), \quad P_0 = \left(-\frac{1}{2} \quad 0\right). \quad (102)$$

Matrix $M^{(V)}$

$$D_n = \left(\frac{3V_0^{(-)}+2V_1^{(-)}}{60}\right), \quad P_n = \left(0 \quad \frac{2V_0^{(-)}+3V_1^{(-)}}{60}\right). \quad (103)$$

Matrix W

$$D_0 = \left(\frac{1}{12}\right), \quad P_0 = \left(0 \quad \frac{1}{12}\right). \quad (104)$$

All these matrices are implemented in the Python package `cylindrical_waveequations`, which uses them to solve the eigenvalue/eigenvector problem described in section 3.1. Thanks to the discretization, the matrices are almost diagonal, which means they can be easily implementable in sparse matrices. This reduces the computational cost and allows us to use these $2N \times 2N$ matrices.